Journal of Building Engineering 98 (2024) 111090

Contents lists available at ScienceDirect

Journal of Building Engineering

journal homepage: www.elsevier.com/locate/jobe

Flexural tensile behaviour of alkali-activated slag-based concrete and Portland cement-based concrete incorporating single and multiple hooked-end steel fibres

Laura Rossi [a,b,*], Maria Paula Zappitelli [c], Ravi A. Patel [a,b], Frank Dehn [a,b]

[a] Institute of Building Materials and Concrete Structures (IMB), Karlsruhe Institute of Technology (KIT), 76131, Karlsruhe, Germany
[b] Material Testing and Research Institute Karlsruhe (MPA), Karlsruhe Institute of Technology (KIT), 76131, Karlsruhe, Germany
[c] Department of Civil Engineering, Engineering College, National University of La Plata (UNLP), Street 1 and 47, La Plata, Argentina

ARTICLE INFO

Keywords:
Multiple hooked-end steel fibres
Alkali-activated concrete
Residual flexural tensile strength
fib model code 2020
FEM

ABSTRACT

In this study, three-point bending tests on notched beams according to EN 14651 have been performed to evaluate the flexural post-cracking behaviour of alkali-activated slag-based concrete (AASC) and Portland cement-based concrete (PCC) incorporating single (3D) and multiple (4D, 5D) hooked-end steel fibres in different volume fractions up to 0.75 %. According to the experimental results, the post-cracking residual flexural strength increases with the increase in the fibre volume fraction for each fibre and concrete matrix type. AASC mixes incorporating 3D and 4D fibres show higher values of residual flexural strength for the same crack opening than PCC mixes with the same fibre type and dosage. Only for the mixes incorporating 5D fibres, steel fibre-reinforced PCC (SFRPCC) mixes outperform steel fibre-reinforced AASC (SFRAASC) mixes in terms of post-cracking behaviour. According to EN 14651, the values of the residual strengths f_{R1} and f_{R3}, corresponding to a crack mouth opening displacement (CMOD) of 0.5 mm and 2.5 mm, respectively, and their corresponding characteristic values f_{R1k} and f_{R3k}, respectively, can be derived from the experimental load-CMOD curves. Following the *fib* Model Code 2020, each mix can then be classified according to the values of f_{R1k} and the f_{R3k}/f_{R1k} ratio. As a result, empirical models have been developed for SFRPCC to predict the values of f_{R1} and f_{R3} and the applicability of such models to SFRAASC is evaluated in this study. Once the values of f_{R1k} and f_{R3k} are known, tensile constitutive models can be derived according to the *fib* Model Code 2020 and used as input parameters for finite element modelling. In this study, the accuracy of the code-based constitutive model to predict the flexural behaviour of SFRAASC and SFRPCC is evaluated using the concrete damage plasticity (CDP) model available in ABAQUS. The numerical model based on the tensile stress-strain curve in the *fib* Model Code 2020 can qualitatively capture the post-cracking behaviour of SFRAASC and SFRPCC incorporating 3D, 4D and 5D at 0.25 % fibre volume fraction, despite overestimating their tensile strength. For higher fibre volume fractions, the CDP model, in conjunction with the mode I parameters derived from the *fib* Model Code 2020, is unable to adequately describe the post-hardening behaviour exhibited by the composites.

* Corresponding author. Institute of Building Materials and Concrete Structures (IMB), Karlsruhe Institute of Technology (KIT), 76131 Karlsruhe, Germany.

E-mail addresses: laura.rossi@kit.edu (L. Rossi), paula.zappitelli@ing.unlp.edu.ar (M.P. Zappitelli), ravi.patel@kit.edu (R.A. Patel), frank.dehn@kit.edu (F. Dehn).

https://doi.org/10.1016/j.jobe.2024.111090
Received 22 July 2024; Received in revised form 4 October 2024; Accepted 16 October 2024
Available online 18 October 2024

1. Introduction

One of the most effective ways to reduce the brittleness of Portland cement-based concrete (PCC) and to enhance its ductility and energy absorption capacity is the use of randomly distributed steel fibres. Steel fibres hinder crack propagation and provide stress transfer by bridging the cracked sections of the concrete member [1–3]. The performance of steel fibre-reinforced cement-based concrete (SFRPCC) depends mainly on the characteristics of the concrete matrix, fibres and their bond properties [2,4,5]. Single hooked-end steel fibres (generally named 3D) have been used widely in applications requiring high tensile strength and modulus of elasticity, such as tunnel linings, joint-less industrial concrete floors, and irrigation and wastewater systems [2,3,5,6]. To improve the crack-bridging efficiency of steel fibres in concrete, multiple hooked-end steel fibres, *i.e.* double hooked-end (4D) and triple hooked-end (5D) fibres, have been recently developed and commercialised. The additional bends at both ends of the fibres enhance the fibre-matrix interface bond, resulting in higher resistance to fibre pull-out and therefore higher tensile and flexural performance of the composite [3,7,8]. Despite being relatively new, 4D and 5D steel fibres and the effect of their novel geometries on the performance of normal- and high-strength traditional cement-based concrete have been the subject of several studies [2,3,9–11]. According to Chen et al. [2], the better fibre-matrix anchorage provided by the multiple hooks at the end of 4D and 5D fibres provides a significant increase in the post-cracking behaviour of steel fibre-reinforced PCC in comparison to PCC incorporating 3D fibres. Venkateshwaran et al. [11] reported a limited effect of the number of hooked ends of the steel fibre on the flexural strength of the composite, but an enhancement of post-cracking residual flexural strength of 9–12 % was observed when 3D fibres were replaced by 5D fibres.

Although steel fibre-reinforced cement-based concrete (SFRPCC) has been widely used for structural and non-structural applications in the last decades, the high embodied CO_2 emissions and energy consumptions related to Portland cement production require the development of more environmentally friendly alternative binders, such as alkali-activated slag-based concrete (AASC) [12–16]. AASC can outperform PCC in terms of mechanical and durability performance [1,13,14,17,18]. However, alkali-activated slag-based concrete can exhibit a more brittle behaviour and higher autogenous shrinkage than PCC, limiting its resistance to crack formation and propagation [1,13,15,19]. Different fibre types have been added to alkali-activated concrete matrices to investigate their effect on the material response under various loading conditions [1,12,15,20–41]. However, studies evaluating the effect of single and multiple hooked-end steel fibres on the composite performance are limited with no research investigating the influence of 4D and 5D steel fibres on the post-cracking behaviour of steel fibre-reinforced alkali-activated slag-based concrete (SFRAASC). El-Hassan and Elkholy [19] focused on alkali-activated slag-fly ash blended concrete reinforced with hybrid steel fibre reinforcement, *i.e.* a combination of single and novel multiple hooked-end steel fibres in different volume fractions. Even though the main mechanical performances, *i.e.* compressive strength, modulus of elasticity, splitting and flexural tensile strength, were evaluated experimentally, the post-cracking flexural behaviour of the composites was not investigated. Koenig et al. [34] evaluated the flexural performance of alkali-activated slag-based concrete (AASC) and cement-based concrete (PCC) incorporating a steel fibre mix of 1/3 short straight fibres and 2/3 single hooked-end steel fibres in different volume fractions by performing three-point bending tests according to EN 14651. Both composites exhibit a post-cracking softening behaviour when reinforced with a fibre volume fraction of 0.60 %. Although SFRAASC shows a higher drop in load than SFRPCC after the peak is achieved, the residual flexural load increases with the increase in CMOD values, while it decreases for SFRPCC. Despite providing new insights on the post-cracking flexural behaviour of steel fibre-reinforced alkali-activated slag-based concrete, the study of Koenig et al. [34] does not evaluate the effect of single hooked-end steel fibres or novel steel fibres on the performances of the composite. Shaikh [42] evaluated the pull-out behaviour of 3D, 4D and 5D fibres in alkali-activated slag-fly ash-based and cement-based mortars. Although alkali-activated slag-fly ash blended mortar exhibits a higher maximum pull-out load, toughness and bond strength than cement-based mortar, the flexural performance of such composites is not investigated.

Evaluating the flexural post-cracking behaviour of SFRAASC experimentally is essential to understand and predict its behaviour as well as to derive tensile constitutive models, *i.e.* stress-strain ($\sigma - \varepsilon$) or stress-crack opening ($\sigma - w$) relationships, which are fundamental for the preliminary design and dimensioning of concrete structural members. The ideal approach to derive the tensile stress-strain ($\sigma - \varepsilon$) relationship for steel fibre-reinforced concrete is to perform direct uniaxial tensile tests. However, direct tensile tests are difficult to perform accurately [43] and the reliability of the results is highly influenced by the fibre type, dosage and orientation. Due to their ease of execution, three-point bending tests on notched beams according to EN 14651 are generally preferred to evaluate the post-cracking behaviour of steel fibre-reinforced composites. From the flexural post-cracking behaviour, several authors [43–46] and design codes, such as the *fib* Model Code 2020 [47], proposed simplified or more accurate tensile constitutive models can be derived for preliminary design or numerical simulations, respectively.

This paper evaluates experimentally the flexural post-cracking behaviour of alkali-activated slag-based concrete and Portland cement-based concrete incorporating single (3D) and multiple (4D and 5D) hooked-end steel fibres in different fibre volume fractions up to 0.75 %. From the experimental Load-CMOD curves the values of the residual flexural strengths f_{R1} and f_{R3} and their corresponding characteristic values f_{R1k} and f_{R3k} are derived to classify the composites according to the *fib* Model Code 2020

recommendations. The applicability to SFRAASC of currently available empirical models for SFRPCC to derive the values of the residual flexural strength f_{R1} and f_{R3} is investigated and a new recalibrated model is proposed for SFRAASC. Finally, the applicability of the linear tensile constitutive laws available in the *fib* Model Code 2020 for SFRAASC and SFRPCC is evaluated. Such tensile constitutive models are used as input parameters for numerical simulations by finite element modelling using the Concrete Damage Plasticity (CDP) model available in ABAQUS.

2. Experimental programme

2.1. Materials

The alkali-activated slag-based concrete matrix was made from ground granulated blast furnace slag (GGBS), water, sodium hydroxide (SH), sodium silicate (SS), and fine and coarse aggregates. To obtain an alkaline solution with a total concentration of 5.3 % Na_2O (expressed as a percentage of slag weight), SH (50 % solid content), SS with a molar ratio $M_s = 3.4$ [mol/mol] and water were pre-mixed 24 h prior casting to reduce heat release [19,34] and prevent fresh concrete rapid setting. CEM I 42.5R was used to produce a reference Portland cement-based concrete. Table 1 shows the chemical composition of the binders.

Glued steel fibres were supplied by NV Bekaert SA. The selected fibres are classified as single hooked-end (Dramix® 3D 65/60 BG), double hooked-end (Dramix® 4D 65/60 BG) and triple hooked-end (Dramix® 5D 65/60 BG) depending on the number of bends at the fibre ends (Fig. 1).

The properties of the steel fibres are given in Table 2. Four different fibre volume fractions – 0 %, 0.25 % (20 kg/m^3), 0.50 % (40 kg/m^3) and 0.75 % (60 kg/m^3) – were added to the reference concrete matrices.

The mix proportions of the plain reference AASC and PCC concrete matrices are given in Table 3. The same binder content, aggregate type, and proportions were used to achieve a similar slump flow class (F4) and 28-day mean compressive strength (Table 3). The twenty mixes, ten for each concrete matrix, are designated as X-YDZ, where X denotes the matrix type (AASC or PCC), YD represents the fibre geometry (3D, 4D or 5D) and Z the fibre volume fraction (0.25 %, 0.50 % and 0.75 %). The reference mixes without fibres are designated as AASC-REF and PCC-REF for alkali-activated slag-based concrete and Portland cement-based concrete, respectively.

2.2. Mixing and sample preparation

The same mixing procedure was followed for all the mixtures. First, the binder was mixed for 90 s with fine and coarse aggregates. Then, the liquid component – the pre-mixed alkaline solution for AASC and water for PCC – was added to the dry components and mixed for two additional minutes to achieve a homogeneous mixture. Finally, before the freshly made concrete was poured into the moulds, steel fibres were added and thoroughly mixed to achieve a total mixing time of 7 min. The equipment used to cast the samples is shown in Fig. 2.

Three cylinders of diameter of 150 mm and height of 300 mm and six 150 mm × 150 mm × 550 mm beams (Fig. 3) were cast for each mixture to assess its 28-day mean compressive strength and flexural response under three-point bending, respectively. The samples were cast from different batches of the same concrete mix. To allow setting and reduce drying shrinkage, plastic covers, damp jute, and plastic foil were placed on the fresh concrete-filled moulds for the first 24 h. After demoulding, the SFRPCC samples were cured underwater (20 ± 2) °C, while the SFRAASC specimens were wrapped in foil [48] and stored in a climate room at (20 ± 2) °C and 65 % relative humidity until the testing date. After a 21-day curing period, a notch measuring 5 ± 1 mm in width and 25 ± 1 mm in depth was sawed at the mid-span of the side face of each beam in accordance with EN 14651.

2.3. Experimental procedure

The 28-mean compressive strength of SFRAASC and SFRPCC was assessed on three cylinders with a diameter of 150 mm and a height of 300 mm, according to EN 12390–3. The post-cracking flexural behaviour was evaluated on six notched beams according to EN 14651. Two rigid steel frames equipped with linear variable differential transducers (LVDTs) were installed at the mid-width of the beam specimens to measure the crack mouth opening displacement (CMOD) at the bottom of the notch on both sides of the beam. The experimental setup is shown in Fig. 4.

Table 1
Chemical composition of GGBS and CEM I.

Binder	CaO [%]	SiO_2 [%]	Al_2O_3 [%]	Fe_2O_3 [%]	MgO [%]	P_2O_5 [%]	K_2O [%]	Na_2O [%]
GGBS	41.84	35.91	10.74	0.39	6.99	0.47	0.40	0.31
CEM I	60.80	19.60	5.25	2.38	1.53	0.13	0.80	0.10

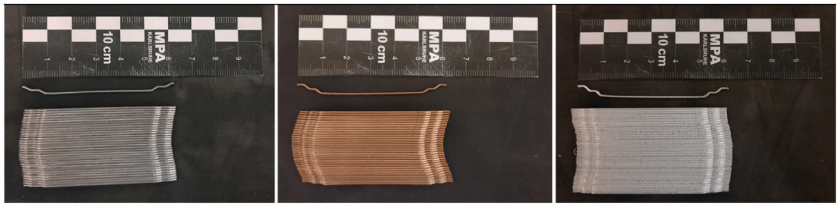

Fig. 1. Single and multiple Dramix® hooked-end steel fibres: (a) 3D, (b) 4D and (c) 5D.

Table 2
Properties of 3D, 4D and 5D hooked-end steel fibres.

Fibre type	Length (l_f) [mm]	Diameter (d_f) [mm]	Aspect ratio (l_f/d_f)	Fibre tensile strength ($\sigma_{f,u}$)[a] [MPa]	Strain at ultimate strength [%]
3D 65/60 BG	60	0.90	65	1160	0.8
4D 65/60 BG	60	0.90	65	1600	0.8
5D 65/60 BG	60	0.90	65	2300	6.0[a]

[a] Provided by the fibre manufacturer (NV Bekaert SA).

Table 3
Mix proportions (in kg/m^3), slump flow class and 28-day compressive strength of the different concrete matrices reference mixes.

Mix	GGBS	CEM	SH	SS	Water	Fine and coarse aggregates			Slump flow class	28-day Compressive strength [MPa]
						0–2 mm	2–8 mm	8–16 mm		
AASC	425	–	50	36	154	660	495	495	F4	50.2
PCC	–	425	–	–	229	660	495	495	F4	49.5

Fig. 2. Mixing and casting equipment: (a) 250-L concrete mixer, (b) weighted mix components, (c) vibration table and beam moulds (top), and freshly mixed alkali-activated slag-based concrete (bottom).

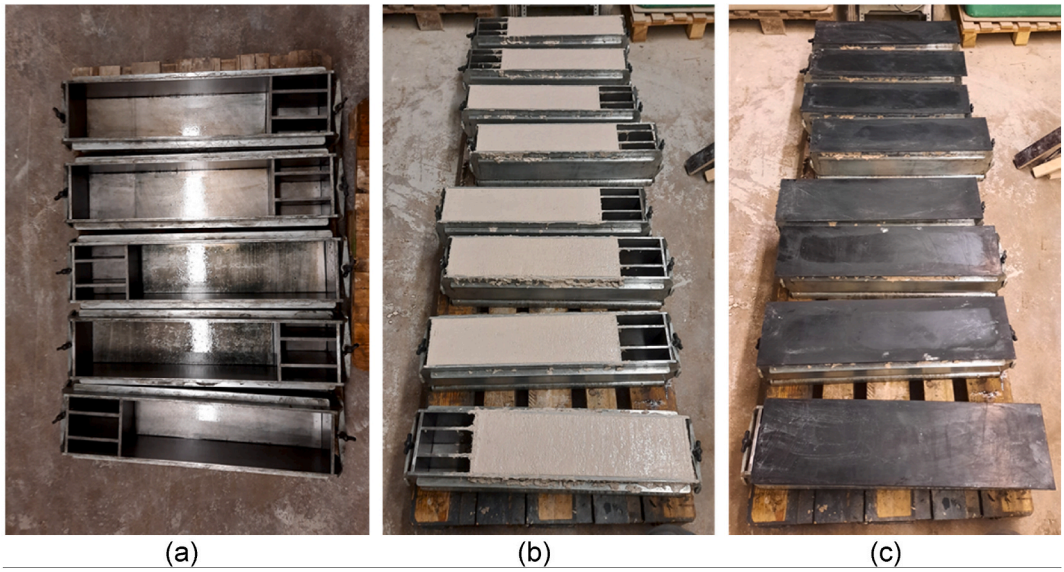

Fig. 3. Beam moulds (a) before casting, (b) after filling with fresh concrete and (c) with plastic covers to minimise drying shrinkage.

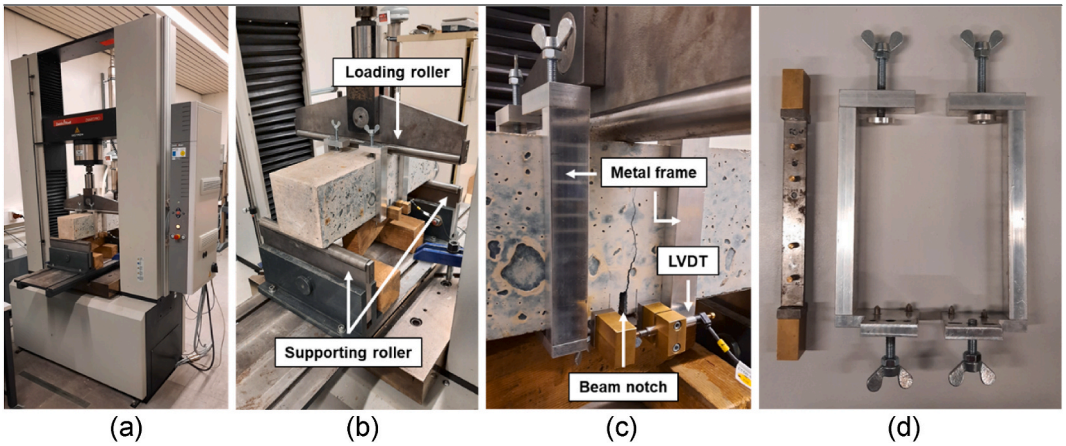

Fig. 4. Three-point bending test experimental setup: (a) testing machine, (b) arrangement of loading, (c) metal frame equipped with LVDTs, and (d) detail of the metal frame.

3. Results and discussion

3.1. Flexural tensile strength

From the experimental load-CMOD curves, the flexural strength corresponding to the Limit of Proportionality (f_{LOP}) and the residual flexural strengths f_{Rj} corresponding to $CMOD_j$ (j = 1, 2, 3, 4) can be derived for each concrete matrix and steel fibre type according to EN 14651 as follows:

$$f_{LOP} = \frac{3 \cdot F_{LOP} \cdot l}{2 \cdot b \cdot h_{sp}^2} \tag{1}$$

$$f_{Rj} = \frac{3 \cdot F_j \cdot l}{2 \cdot b \cdot h_{sp}^2} \quad (2)$$

where F_{LOP} is the load corresponding to the Limit of Proportionality (LOP), *i.e.* the highest load value in the CMOD range from 0 to 0.05 mm, F_j is the load corresponding to $CMOD_j$ (j = 1, 2, 3, 4), *i.e.* 0.5 mm ($CMOD_1$), 1.5 mm ($CMOD_2$), 2.5 mm ($CMOD_3$) and 3.5 mm ($CMOD_4$), respectively, and l, b, and h_{sp} are the span of the concrete beam specimen (500 mm in this study), the width of the sample (150 mm in this study), the distance between the tip of the notch and the top of the beam (125 mm in this study). Additionally, according to the *fib* Model Code 2020 [47], the values of the characteristic residual flexural tensile strengths f_{R1k} and f_{R3k}, corresponding to $CMOD_1 = 0.5$ mm and $CMOD_3 = 2.5$ mm respectively, can be derived as follows:

$$f_{Rjk} = f_{Rj} - k \cdot \sigma \quad (3)$$

where f_{Rj} is the residual flexural strength defined in Eq. (2), k is a constant linked to the number n of samples tested ($k = 1.770$ when $n = 6$, as in this study) and σ is the standard deviation of the mean residual flexural strength f_{Rj}.

3.2. Post-cracking flexural tensile behaviour

3.2.1. Classification according to the fib Model Code 2020

The characteristic flexural tensile strengths f_{R1k} and f_{R3k} and their ratio, *i.e.* f_{R3k}/f_{R1k}, are used to classify the post-cracking flexural tensile behaviour of steel fibre-reinforced concrete composites through a number and a letter, respectively. The number (1.0, 1.,5, 2.0, 2.5, 3.0, 4.0, 5,0, 6.0, 7.0, 8.0 [MPa]) denotes the f_{R1k} class, corresponding to the characteristic strength at serviceability limit state (SLS), while the letter (a, b, c, d and e) corresponds to specific values of the f_{R3k}/f_{R1k} ratio, defined as follows:

Table 4
Experimental values of f_c, E_c, f_{LOP}, f_{Rj} (j = 1, 2, 3, 4), f_{R1k}, f_{R3k}/f_{R1k} and the classification of each mix according to the *fib* Model Code 2020.

Mix	f_c [MPa]	E_c [GPa]	f_{LOP} [MPa]	f_{R1} [MPa]	f_{R2} [MPa]	f_{R3} [MPa]	f_{R4} [MPa]	f_{R1k} [MPa]	f_{R3k}/f_{R1k} [MPa]	Class
AASC-REF	40.9 (0.86)	27.6 (0.64)	5.02 (0.11)	0.30 (0.10)	–	–	–	–	–	–
PCC-REF	45.2 (0.64)	27.9 (0.55)	4.59 (0.23)	0.29 (0.08)	–	–	–	–	–	–
AASC-3D25	43.8 (0.35)	28.1 (0.42)	6.22 (0.26)	2.93 (0.51)	3.40 (0.70)	3.45 (0.87)	3.36 (0.88)	2.03	0.94	2c
AASC-3D50	44.8 (0.84)	28.2 (0.61)	5.92 (0.47)	5.66 (0.84)	7.00 (1.03)	6.93 (1.02)	6.65 (0.89)	4.17	1.23	4d
AASC-3D75	48.3 (0.73)	30.0 (1.09)	5.66 (0.38)	6.88 (1.21)	8.07 (1.28)	8.03 (1.13)	7.66 (0.90)	4.73	1.27	4d
PCC-3D25	39.0 (1.11)	27.5 (0.81)	4.52 (0.31)	2.88 (0.39)	3.16 (0.41)	3.05 (0.40)	2.86 (0.39)	2.18	1.08	2d
PCC-3D50	38.5 (1.36)	26.7 (0.54)	4.66 (0.18)	5.41 (0.58)	6.29 (1.04)	6.07 (0.96)	5.66 (0.83)	4.38	1.00	4c
PCC-3D75	40.1 (0.43)	28.2 (1.15)	4.85 (0.38)	6.34 (0.77)	7.53 (0.92)	7.28 (0.82)	6.66 (0.93)	4.98	1.17	4d
AASC-4D25	45.4 (0.76)	28.1 (0.80)	5.30 (0.27)	3.15 (1.13)	3.70 (1.12)	3.91 (1.08)	3.26 (0.62)	1.14	1.75	1e
AASC-4D50	44.2 (0.80)	28.2 (0.50)	5.46 (0.37)	5.55 (1.23)	7.06 (1.32)	6.91 (0.87)	6.48 (0.57)	3.38	1.59	3e
AASC-4D75	44.3 (2.45)	27.4 (0.39)	5.79 (0.25)	7.86 (0.83)	8.87 (0.38)	8.05 (0.35)	7.40 (0.47)	6.39	1.16	6d
PCC-4D25	40.3 (0.86)	27.0 (0.85)	4.13 (0.23)	2.81 (0.26)	3.90 (0.40)	4.14 (0.50)	3.98 (0.38)	2.36	1.38	2e
PCC-4D50	43.6 (1.09)	27.4 (0.30)	4.73 (0.32)	5.53 (0.91)	7.68 (1.10)	7.05 (1.00)	6.85 (1.12)	3.93	1.35	3e
PCC-4D75	45.1 (1.53)	27.7 (0.22)	4.85 (0.39)	6.16 (1.79)	7.08 (1.28)	6.66 (1.13)	5.78 (1.06)	2.99	1.56	2,5e
AASC-5D25	45.2 (0.47)	27.7 (0.36)	5.83 (0.40)	2.44 (0.57)	2.94 (0.64)	3.07 (0.60)	3.04 (0.47)	1.44	1.40	1e
AASC-5D50	52.6 (3.16)	28.8 (0.68)	5.84 (0.43)	6.23 (1.69)	8.44 (2.02)	7.88 (1.39)	7.02 (1.37)	3.24	1.68	3e
AASC-5D75	48.4 (1.11)	29.4 (1.12)	5.86 (0.34)	7.66 (0.55)	8.69 (0.90)	8.30 (1.00)	7.57 (1.09)	6.74	0.97	6c
PCC-5D25	45.2 (2.20)	27.4 (0.52)	4.52 (0.25)	3.11 (0.53)	4.11 (0.68)	4.27 (0.83)	4.49 (0.71)	2.17	1.29	2d
PCC-5D50	44.7 (0.86)	27.4 (0.61)	4.56 (0.44)	5.10 (1.09)	6.63 (1.00)	5.98 (0.65)	5.58 (0.55)	3.17	1.53	3e
PCC-5D75	48.2 (1.39)	27.5 (0.96)	5.19 (0.58)	8.23 (1.38)	9.58 (0.88)	8.73 (0.45)	7.87 (0.59)	5.78	1.37	5e

v_f = fibre volume fraction. The values in the brackets represent the standard deviation.

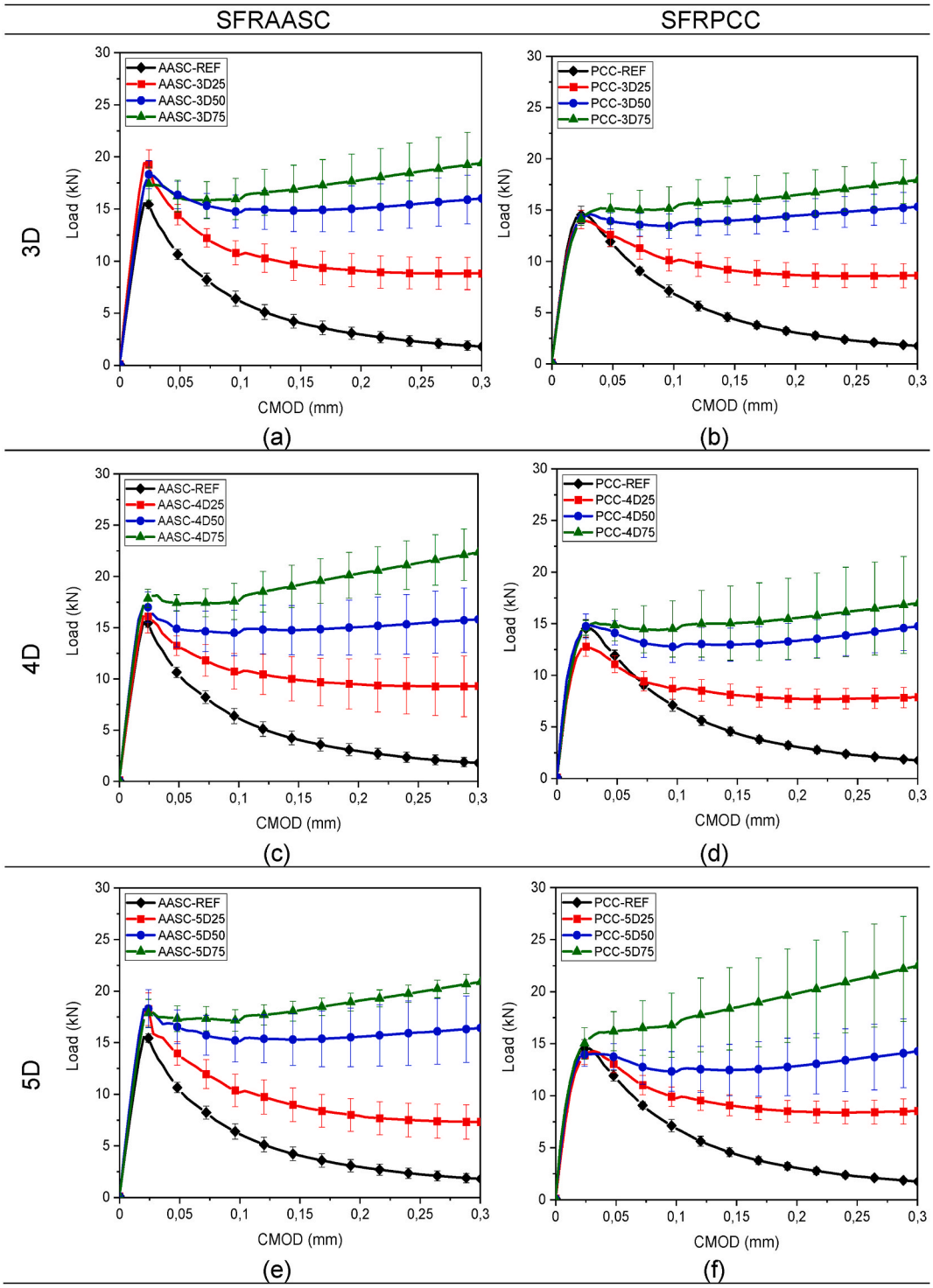

Fig. 5. Load-CMOD curves and relative standard deviation of SFRAASC and SFRPCC mixes reinforced with (a, b) 3D fibres, (c, d) 4D fibres, and (e, f) 5D fibres, respectively, at different volume fractions up to a CMOD = 0.30 mm.

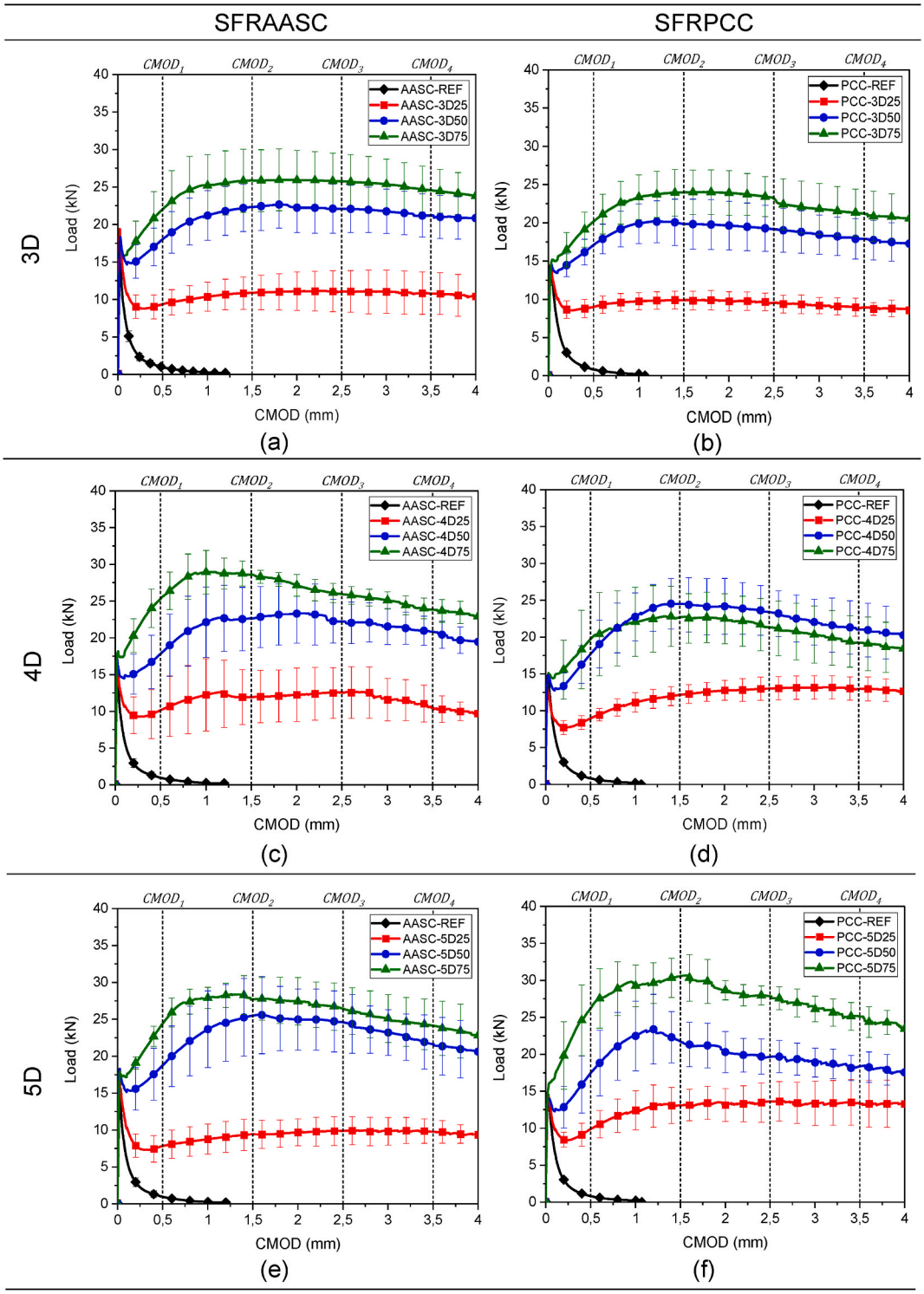

Fig. 6. Average load-CMOD curves and relative standard deviation of SFRAASC and SFRPCC mixes reinforced with (a, b) 3D fibres, (c, d) 4D fibres, and (e, f) 5D fibres, respectively, at different volume fractions.

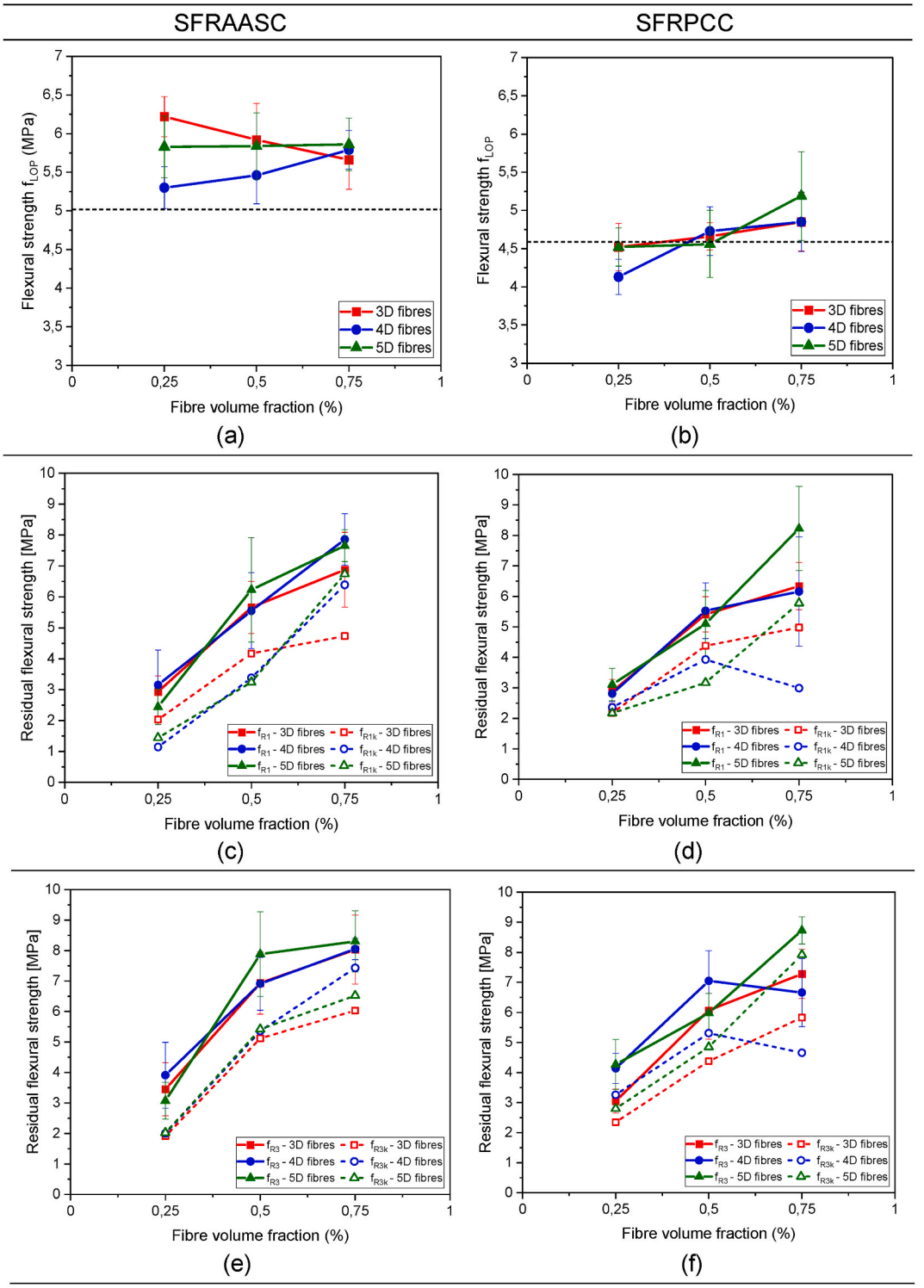

Fig. 7. Correlation between the fibre volume fraction and (a, b) the flexural strength f_{LOP}, (c, d) the residual flexural strength f_{R1} and f_{R1k}, and (e, f) the residual flexural strength f_{R3} and f_{R3k}, for each fibre geometry for SFRAASC and SFRPCC mixes, respectively. The dashed line in (a, b) indicates the value of f_{LOP} for the reference mix.

a if $0.5 < f_{R3k}/f_{R1k} < 0.7$

b if $0.7 \leq f_{R3k}/f_{R1k} < 0.9$

c if $0.9 \leq f_{R3k}/f_{R1k} < 1.1$

d if $1.1 \leq f_{R3k}/f_{R1k} < 1.3$

e if $1.3 \leq f_{R3k}/f_{R1k}$

Table 4 summarises the values of the 28-day mean cylindrical compressive strength (f_c), the flexural strength f_{LOP}, the residual flexural strength f_{Rj} (j = 1, 2, 3, 4) corresponding to CMOD values of 0.5 mm, 1.5 mm, 2.5 mm and 3.5 mm, respectively, the characteristic residual flexural strengths f_{R1k} and f_{R3k}, and the material class according to the *fib* Model Code 2020. In addition, the values of 28-day modulus of elasticity (E_c), evaluated by the authors in a previous study on samples obtained from different batches of the same concrete mixes [48], are given in Table 4.

3.2.2. Effect of the concrete matrix properties on f_{LOP}

According to the results summarised in Table 4, the 28-day compressive strength has a different effect on f_{LOP} for SFRAASC and SFRPCC. For SFRPCC, a direct correlation between the compressive strength and f_{LOP} can be observed, *i.e.* f_{LOP} generally increases with the increase of the compressive strength. For all fibre types, the increase in compressive strength with the fibre content increases f_{LOP}. For SFRAASC, the opposite can be observed, *i.e.* the compressive strength and f_{LOP} are indirectly correlated. For 3D fibres, the increase in compressive strength with the increase in the fibre volume fraction corresponds to a decrease in f_{LOP}, while for 4D fibres a decrease in compressive strength corresponds to an increase in f_{LOP}. For 5D fibres, variations in the compressive strength do not affect the values of f_{LOP}. Although for SFRPCC the highest value of f_{LOP} corresponds to the highest value of compressive strength (PCC-5D75), the same does not apply for SFRAASC, as the highest value of f_{LOP} is achieved by the mix AASC-3D25, while the highest value of compressive strength is observed for the mix AASC-5D50.

Although alkali-activated concrete generally exhibits a lower modulus of elasticity than traditional cement-based concrete [49], as also shown in Table 4 for the reference mixes, the incorporation of hooked-end steel fibres at different volume fractions enhances the modulus of elasticity of SFRAASC, which is higher than the one of SFRPCC for each fibre type (Table 4). However, no clear correlation between the modulus of elasticity and f_{LOP} can be seen. As for the compressive strength, the highest value of f_{LOP} does not necessarily correspond to the highest value of the modulus of elasticity. For SFRPCC the highest value of f_{LOP} is achieved by the mix PCC-5D75, while the highest value of the modulus of elasticity is achieved by the mix PCC-3D75. For SFRAASC the highest value of f_{LOP} is achieved by the mix AASC-3D25, while the highest value of E_c is observed for the mix AASC-3D75. Although the modulus of elasticity is generally directly correlated to the compressive strength of the material, discrepancies in the correlation between the compressive strength and f_{LOP} and between the modulus of elasticity and f_{LOP} could be related to the sample preparation, *i.e.* different concrete batches of the same mix.

3.2.3. Effect of fibre type and volume fraction on f_{LOP}

Fig. 5 shows the experimental load-CMOD curves up to a CMOD value of 0.3 mm to evaluate the effect of the fibre type and volume fraction on the flexural strength f_{LOP} of both SFRAASC and SFRPCC. Single and multiple hooked-end steel fibres generally have a limited effect on f_{LOP}, which is mainly dependent on the compressive strength and load-bearing capacity of the plain concrete matrix [1]. This can be seen for SFRPCC mixes, as the f_{LOP} decreases in comparison to the reference plain concrete for each fibre type at a volume fraction of 0.25 %, achieving the lowest value for the mix PCC-4D25 (−10 % in comparison to PCC-REF), while it increases with the increase in the fibre volume fraction up to 0.75 % for each fibre type, with PCC-5D75 showing the highest value (+13.1 % in comparison to PCC-REF). For SFRAASC, the value of f_{LOP} is higher for each concrete mix incorporating steel fibres in contrast to the reference mix, although different correlations between the values of f_{LOP} and the fibre type and dosage can~~not~~ be seen. For 3D fibres, f_{LOP} reaches its higher value at the lower fibre content (AASC-3D25) and decreases with the increase in the fibre volume fraction. For 4D fibres, f_{LOP} increases with the increase in the fibre volume fraction, while for 5D fibres, all volume fractions exhibits similar values of f_{LOP}.

Although for SFRPCC mixes the fibre type and dosage seem to have no clear and significant effect on the flexural strength f_{LOP}, with the concrete matrix playing a more relevant role, for SFRAASC mixes, the incorporation of steel fibres enhances f_{LOP}, with 3D fibres providing the highest increment (+23.9 % than AASC-REF) at the lowest fibre content.

3.2.4. Effect of the concrete matrix properties on the post-peak response

As shown in Table 4, the values of the residual flexural strengths f_{R1} and f_{R3} increase with the fibre volume fraction for each fibre and concrete matrix type. Although the fibre geometry and dosage have a more significant effect on the post-cracking flexural

behaviour of the composite, a clear correlation between f_{R1} and f_{R3} and the concrete matrix properties can be seen, *i.e.* f_{R1} and f_{R3} generally increase with the increase in compressive strength and modulus of elasticity for SFRAASC and SFRPCC. Only for SFRAASC incorporating 4D fibres, a decrease in compressive strength and modulus of elasticity with the fibre volume fraction results in an increase of f_{R1} and f_{R3}. However, as observed for f_{LOP}, the highest values of compressive strength and modulus of elasticity do not necessarily correspond to the highest values of f_{R1} and f_{R3}. Once the concrete matrix achieves the peak flexural strength, the post-cracking behaviour is mainly governed by the steel fibres, as the crack starts propagating and the stresses cannot be sustained by the cracked concrete matrix.

3.2.5. Effect of fibre type and volume fraction on the post-peak response

Fig. 6 shows the experimental load-CMOD curves obtained for each fibre and concrete matrix type. Both plain concrete reference mixes exhibit a brittle failure, *i.e.* the load abruptly drops after achieving its maximum value, due to the initial cracking of the matrix and the absence of fibres transferring stresses through the surfaces of the crack [50].

When steel fibres are introduced into the concrete matrices, a more ductile post-cracking behaviour can be observed for both SFRAASC and SFRPCC mixes (Fig. 6). With the increment of the fibre volume fraction from 0.25 % to 0.50 %, the increased number of fibres at the crack surface mitigates the post-peak drop of load and enhances the post-cracking response, resulting in higher residual flexural load and corresponding strength, for each matrix and fibre type. The additional increase of fibre volume fraction from 0.50 % to 0.75 % leads to a post-cracking deflection hardening behaviour, in which the post-cracking load drop is completely neutralised and the fibres at the crack surface can bear and transfer the bending tensile stresses through the crack surfaces to the matrix. Steel fibre incorporation significantly affects the post-peak descending branch of the load-CMOD curve and the values of the residual flexural strengths. Although the increase of the fibre volume fraction from 0.25 % to 0.50 % corresponds to an almost doubled increase in the residual flexural strength, a further increase of fibre content from 0.50 % to 0.75 % volume fraction provides a limited enhancement of the residual flexural strengths. SFRAASC mixes outperforming SFRPCC mixes when reinforced with 3D and 4D fibres, whereas with 5D fibres, SFRPCC mixes exhibit higher values of residual flexural strength as shown in Fig. 6 and Table 4.

Fig. 7 shows the correlation between the fibre volume fraction and the values of f_{LOP}, f_{R1} and f_{R3}, and the corresponding characteristic values f_{R1k} and f_{R3k}, for each concrete matrix and fibre type. As shown in Fig. 9a and 9b, SFRAASC exhibits higher flexural strength (f_{LOP}) than SFRPCC for each fibre type and volume fraction. Single and multiple hooked-end steel fibres improve the initial cracking load of SFRAASC due to the early activation of their crack bridging effect possibly due to micro-cracking induced by the higher autogenous shrinkage compared to SFRPCC mixes [34]. For both SFRAASC and SFRPCC, however, the increase of fibre volume fraction has a limited effect on the flexural strength f_{LOP}, which slightly increases for SFRPCC and slightly decreases for SFRAASC, for each fibre type, with the increase of the fibre dosage.

However, for SFRAASC, an improvement of f_{LOP} in comparison to the plain reference mix can be seen already at the lowest fibre volume fraction (0.25 %) for each fibre type. For SFRPCC improvements can be seen at a higher volume fraction, i.e. 0.50 %, whereas at 0.25 % fibre content, lower values of f_{LOP} than the reference mix are observed regardless of the fibre geometry.

Table 5
Empirical equations to predict the residual flexural strengths of SFRPCC.

Author	Empirical equations
Moraes Neto et al. [52]	$f_{R1} = 7.5 \cdot (RI_v)^{0.8}$ $f_{R3} = 6.0 \cdot (RI_v)^{0.7}$
Venkateshwaran et al. [11]	$f_{R1} = \Psi \cdot \left(0.32 \cdot (f_{cm})^{1/2} + 6.214 \cdot RI_v + 0.034 \cdot N^2\right)$ $f_{R3} = \Psi \cdot \left(0.30 \cdot (f_{cm})^{1/2} + 7.629 \cdot RI_v + 0.373 \cdot N^2\right)$
Chen et al. [2]	$f_{R1} = 0.09120 \cdot \left(f_{cu,0}\right)^{2/3} \cdot \left[1 + \left(0.0899 \cdot l_f + 1.29476 \cdot (N)^{1/2}\right) \cdot RI_v\right]$ $f_{R3} = 0.08594 \cdot \left(f_{cu,0}\right)^{2/3} \cdot \left[1 + \left(0.0382 \cdot l_f + 4.60597 \cdot (N)^{1/2}\right) \cdot RI_v\right]$
Oettel et al. [53]	$f_{R1} = \frac{1}{0.37} \cdot k \cdot v_f \cdot (1 - k \cdot v_f) \cdot \frac{f_{LOP}}{0.39} \cdot \zeta_1 \cdot \eta_v$ $f_{R3} = \frac{1}{0.37} \cdot k \cdot v_f \cdot (1 - k \cdot v_f) \cdot \frac{f_{LOP}}{0.39} \cdot \zeta_3 \cdot \eta_v$
Faccin et al. [51]	$f_{R1} = 2.7 \cdot (f_{cm})^{1/2} \cdot \left(\frac{l_f}{d_f}\right)^{0.8} \cdot (v_f)^{0.9}$ $f_{R3} = 0.5 \cdot (f_{cm})^{2/3} \cdot \left(\frac{l_f}{d_f}\right) \cdot (v_f)^{0.85}$

$RI_v = v_f \cdot (l_f/d_f)$ = fibre reinforcing index, v_f = fibre volume fraction [%], l_f = fibre length [mm], d_f = fibre diameter [mm], $\Psi = (1 + l_f/100)^{1/2}$ = factor accounting for the fibre length, f_{cm} = cylindrical compressive strength, N = number of bends at the fibre ends ($N = 1$ for 3D fibres, $N = 1.5$ for 4D fibres and $N = 2$ for 5D fibres), $f_{cu,0}$ = cubic compressive strength of plain concrete, $k = (l_f/d_f) \cdot \chi$, $\chi = 0.3$ for hooked-end steel fibres, $\zeta_1 = 1.18 - 7.5 l_f/1000$, $\zeta_3 = 0.42 + 7.5 l_f/1000$, $\eta_v = 1/(0.7 - 0.2 v_f)$.

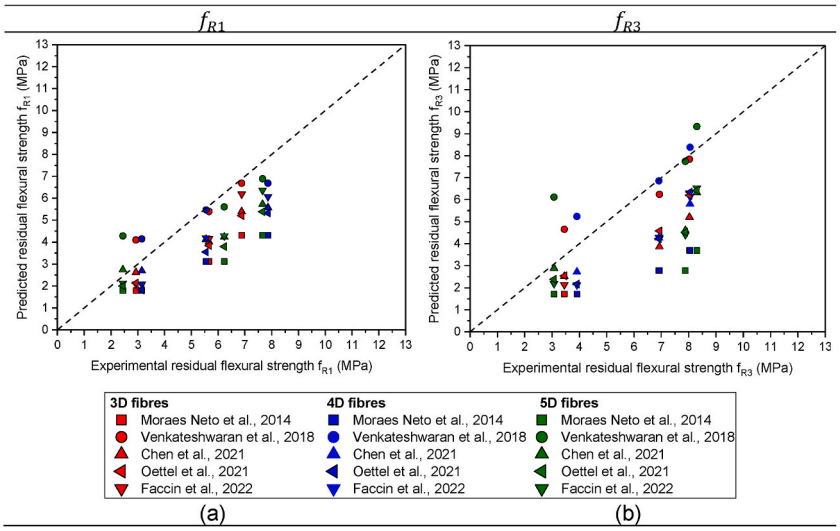

Fig. 8. Correlation between the experimental and the predicted values of (a) f_{R1} and (b) f_{R3} for SFRAASC incorporating 3D, 4D and 5D steel fibres.

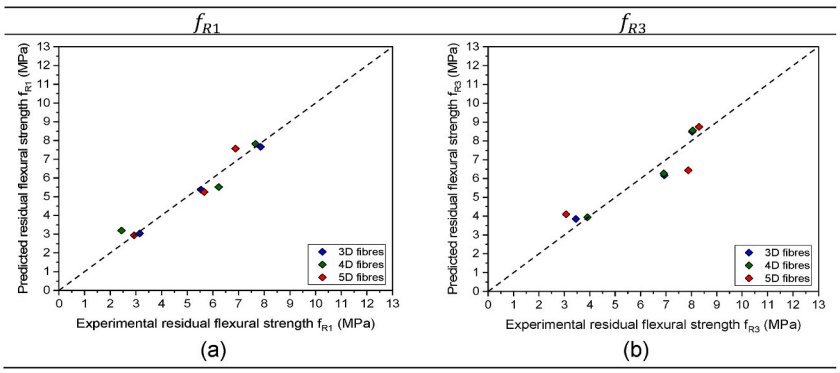

Fig. 9. Correlation between the experimental and the predicted values of (a) f_{R1} and (b) f_{R3} for SFRAASC incorporating 3D, 4D and 5D steel fibres obtained by using the newly calibrated correlations.

Table 6
IAE values of the currently available empirical models used to predict the residual flexural strengths f_{R1} and f_{R3} of SFRAASC.

Empirical model	IAE [%]					
	3D		4D		5D	
	f_{R1}	f_{R3}	f_{R1}	f_{R3}	f_{R1}	f_{R3}
Moraes Neto et al. [52]	40.5	55.5	44.4	56.6	43.6	57.5
Venkateshwaran et al. [11]	10.6	11.3	13.6	9.1	19.8	21.9
Chen et al. [2]	22.3	37.1	25.2	32.2	25.9	28.3
Oettel et al. [53]	27.7	27.6	35.5	32.5	31.5	30.8
Faccin et al. [51]	19.6	31.2	25.5	33.5	21.8	31.8

For both SFRAASC and SFRPCC, the values of the residual strengths f_{R1} and f_{R3} increases with the increase of the fibre volume fraction for each type of fibre, with only PCC mixes incorporating 4D fibres showing a decrease of f_{R3} when the fibre volume fraction increases from 0.50 % to 0.75 %. Alkali-activated slag-based concrete mixes reinforced with 3D fibres outperform PCC mixes incorporating the same fibre type, with f_{R1} and f_{R3} showing higher values than SFRPCC, as also shown in Table 4. When 4D fibres are added, SFRAASC mixes show higher values of f_{R1} than SFRPCC mixes for each volume fraction. For all mixes, except for the mix AASC-4D75, SFRAASC shows lower value of f_{R3} compared to SFRPCC. When 5D fibres are considered, the PCC mixes outperform the AASC mixes, with only the mix AASC-5D50 showing higher values of f_{R1} and f_{R3} than PCC. The characteristic values f_{R1k} and f_{R3k} follow a similar trend as the corresponding mean experimental values f_{R1} and f_{R3} for each concrete matrix and fibre types, *i.e.* they generally increase with the fibre content. However, the values of f_{R1k} and f_{R3k} are significantly affected by the variability of the experimentally

determined values of f_{R1} and f_{R3}. Thus, the mixes showing the highest values of f_{R1} and f_{R3} do not necessarily show the highest values of f_{R1k} and f_{R3k}. For example, PCC-3D75 and PCC-4D75 show similar values of f_{R1}, 6.34 and 6.16 MPa, respectively, while the value of f_{R1k} varies significantly (4.98 and 2.99 MPa, respectively). AASC-4D75 and AASC-5D75 show similar values of f_{R3} (8.05 and 8.30 MPa, respectively) but different values of f_{R3k} (7.4 and 6.5 MPa, respectively). Additional investigations are needed to evaluate the effect of the variability of the results on the performance of the composite, as significant variability can nullify the effect of increased fibre volume fractions.

3.3. Empirical models to derive the residual flexural strengths f_{R1} and f_{R3}

The ability to predict the values of the characteristic residual flexural strengths f_{R1k} and f_{R3k} based on the concrete matrix compressive strength and the fibre geometry and volume fraction reduces the number of experiments required to evaluate the material performance, enabling preliminary structural design and verification in reduced time and cost. Several authors [11,43,51–53] proposed empirical models to predict the residual flexural strengths f_{R1} and f_{R3} rather than their corresponding characteristic values f_{R1k} and f_{R3k} by knowing the compressive strength of the reference plain concrete and the fibre geometry and volume fraction. This is mostly because the previous version of the *fib* Model Code (*fib* Model Code 2010) required the determination of the characteristic values f_{R1k} and f_{R3k} solely for material classification rather than for design purposes. Additionally, experimental data in the literature rarely include the standard deviation from the mean values of f_{R1} and f_{R3}, making calculating the corresponding characteristic values more challenging. Table 5 summarises the currently available empirical equations to predict f_{R1} and f_{R3} developed for steel fibre-reinforced Portland cement-based concrete (SFRPCC).

Fig. 8 shows the correlation between the experimental and the predicted values of the residual flexural strengths f_{R1} and f_{R3} for SFRAASC calculated using the empirical equations collected in Table 5. To evaluate the accuracy of prediction of each empirical equation, the Integral Absolute Error (IAE) is introduced as follows:

$$\mathrm{IAE} = \frac{\sum |Q_i - P_i|}{\sum Q_i} \cdot 100 \tag{4}$$

where Q_i is the experimental data and P_i is the predicted value. Table 6 summarises the values of IAE for each empirical model collected in Table 5 and for each fibre type investigated in this study. The lower the values of IAE, the more accurate the prediction. As shown in Table 6, the correlations proposed by Moraes Neto et al. [52] and Venkateshwaran et al. [11] are the ones showing the highest and the lowest values of IAE, respectively.

The correlations proposed by Moraes Neto et al. [52] correlate the residual flexural strengths f_{R1} and f_{R3} only with the fibre reinforcing index RI_v without considering the fibre geometry, in particular, the number of hooks at the fibre ends, resulting in an underestimation of both the residual flexural strengths for SFRAASC incorporating single (3D) and multiple hooked-end steel fibres (4D and 5D). The equations proposed by Venkateshwaran et al. [11] can predict the values of the residual strengths f_{R1} and f_{R3} for SFRAASC quite accurately for each fibre type.

Although calibrated for SFRPCC, the empirical equations proposed by Venkateshwaran et al. [11] show the best accuracy of prediction also for SFRAASC. The general form of such correlations is given in Eqs. (5) and (6), where A, B, C, D, E and F are the coefficients to be recalibrated using the experimental data generated in this study for SFRAASC.

$$f_{R1} = \Psi \cdot \left(A \cdot (f_{cm})^{1/2} + B \cdot RI_v + C \cdot N^2 \right) \tag{5}$$

$$f_{R3} = \Psi \cdot \left(D \cdot (f_{cm})^{1/2} + E \cdot RI_v + F \cdot N^2 \right) \tag{6}$$

with $\Psi = \left(1 + l_f/100\right)^{1/2}$, f_{cm} is the mean cylindrical compressive strength, $RI_v = v_f \cdot \left(l_f/d_f\right)$ is the fibre reinforcing index (v_f = fibre volume fraction, l_f = fibre length, d_f = fibre diameter) and N is the number of hooked ends of the steel fibres ($N = 1$ for 3Dfibres, $N = 1.5$ for 4D fibres and $N = 2$ for 5D fibres).

The coefficients A – F have been recalibrated by minimising the objective function defined as the mean of the sum of the squares of the difference between the experimental and predicted values. The Generalised Reduced Gradient (GRG) non-linear optimisation algorithm available in Microsoft Excel® Solver add-in has been used to carry out the recalibration. The newly calibrated equations are:

$$f_{R1} = \Psi \cdot \left(0.063 \cdot (f_{cm})^{1/2} + 10.991 \cdot RI_v + 0.064 \cdot N^2 \right) \tag{7}$$

Table 7
IAE values of the original and newly calibrated empirical correlations.

Empirical model	IAE [%]					
	3D		4D		5D	
	f_{R1}	f_{R3}	f_{R1}	f_{R3}	f_{R1}	f_{R3}
Venkateshwaran et al. [11]	10.6	11.3	13.6	9.1	19.8	21.9
New correlations	7.1	8.8	3.5	6.2	3.4	15.2

Table 8
Values of the coefficients $A - F$ proposed by Venkateshwaran et al. and the newly calibrated ones.

Empirical model	Coefficient					
	f_{R1k}			f_{R3k}		
	A	B	C	D	E	F
Venkateshwaran et al. [11]	0.226	5.447	−0.149	0.201	6.830	0.182
New correlations	−0.103	10.466	0.053	−0.029	11.115	0.069

Table 9
IAE values of the original and newly calibrated empirical correlations.

Empirical model	IAE [%]					
	3D		4D		5D	
	f_{R1k}	f_{R3k}	f_{R1k}	f_{R3k}	f_{R1k}	f_{R3k}
Venkateshwaran et al. [11]	13.2	15.3	31.6	19.2	29.0	19.5
New correlations	20.9	13.0	10.2	10.0	12.5	11.9

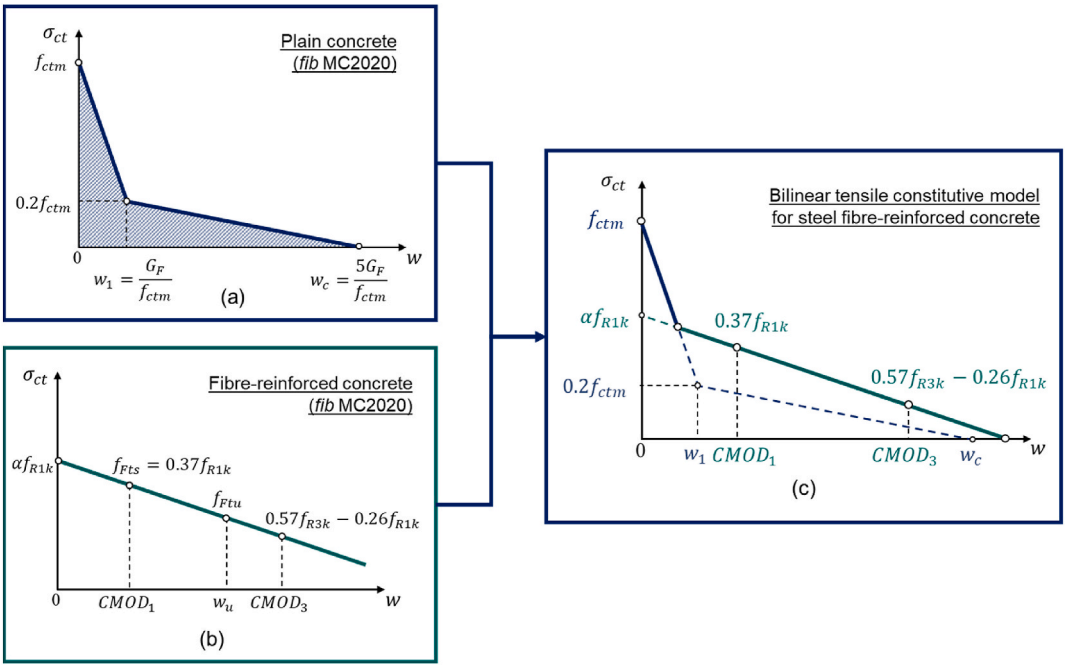

Fig. 10. Tensile constitutive models for (a) plain concrete and (b) steel fibre-reinforced concrete according to the *fib* Model Code 2020. The post-cracking bilinear tensile stress-crack opening for steel fibre-reinforced concrete is described by (c).

$$f_{R3} = \Psi \cdot \left(0.169 \cdot (f_{cm})^{1/2} + 11.037 \cdot RI_v + 0.059 \cdot N^2\right) \tag{8}$$

Table 7 shows the IAE values for the newly calibrated coefficients, while Fig. 9 shows the correlation between the experimental and predicted values of f_{R1} and f_{R3} obtained by using the newly proposed empirical models. Significant improvements in the accuracy of the prediction of f_{R1} can be observed for all fibre types, whereas minor improvements can be seen for f_{R3}.

Venkateshwaran et al. [11] proposed empirical equations to derive the characteristic residual flexural strengths f_{R1k} and f_{R3k} based on the same general correlations proposed in Eq. (5) and Eq. (6). Following the same approach used in this section for f_{R1} and f_{R3}, the coefficients of such equations can be recalibrated using the characteristic values f_{R1k} and f_{R3k} calculated from the experimental values obtained in this study. The newly recalibrated equations can be written as follows:

$$f_{R1k} = \Psi \cdot \left(-0.103 \cdot (f_{cm})^{1/2} + 10.466 \cdot RI_v + 0.053 \cdot N^2\right) \tag{9}$$

$$f_{R3k} = \Psi \cdot \left(-0.029 \cdot (f_{cm})^{1/2} + 11.115 \cdot RI_v + 0.069 \cdot N^2 \right) \quad (10)$$

Tables 8 and 9 summarise the coefficients $A - F$ proposed by Venkateshwaran et al. [11] and the newly calibrated ones, and their corresponding IAE values, respectively. As observed for the residual flexural strength f_{R1} and f_{R3}, the contribution of the compressive strength and the number of bends at the end of the fibre is less relevant for SFRAASC than SFRPCC, while the fibre reinforcing index RI_v seems to play a more significant effect. Negative values of the coefficients A and D could be the result of the limited amount of data used for the calibration and their limited variability. The experimental data used by Venkateshwaran et al. [11] exhibit a 28-day compressive strength ranging from 28.1 to 56.1 MPa, while in this study the 28-day compressive strength of SFRAASC ranges from 43.8 to 52.6 MPa. Thus, additional experimental data are needed to validate such conclusion.

As shown in Table 9, the values of the IAE decreases for each fibre type, proving the need of further calibration of currently existing empirical equations for alternative binders such as alkali-activated slag-based concrete incorporating steel fibres.

3.4. Verification of the fib Model Code 2020 tensile constitutive model

3.4.1. fib Model Code 2020 tensile costitutive model

A bilinear tensile stress-crack opening constitutive model describing the tensile post-cracking behaviour of steel fibre-reinforced concrete can be derived from three-point bending tests (Fig. 10c). According to the *fib* Model Code 2020 [47], the first branch of the curve can be derived from the post-cracking response of plain concrete under uniaxial tension (Fig. 10a).

The stress-crack opening relationship is described as follows:

$$\sigma_{ct} = \begin{cases} f_{ctm} \cdot (1 - 0.8 \cdot (w/w_1)), w < w_1 \\ f_{ctm} \cdot (0.25 - 0.05 \cdot (w/w_1)), w_1 < w \leq w_c \end{cases} \quad (11)$$

where $w_1 = G_F/f_{ctm}$ and $w_c = 5 \cdot G_F/f_{ctm}$ are the crack openings at $\sigma_{ct} = 0.20 \cdot f_{ctm}$ and $\sigma_{ct} = 0$, respectively, and f_{ctm} and G_F are the tensile strength and the fracture energy, respectively. For plain concrete, f_{ctm} and G_F can be derived as follows:

$$f_{ctm} = 1.8 \cdot \ln(f_{ck}) - 3.1 \quad (12)$$

$$G_F = 85 \cdot (f_{ck})^{0.15} = 85 \cdot (f_{cm} - 8)^{0.15} \quad (13)$$

where f_{ck} and f_{cm} represent the characteristic and mean cylindrical compressive strength of the plain concrete, respectively. The second branch of the tensile constitutive model is defined by the *fib* Model Code 2020 for steel fibre-reinforced cement-based concrete (SFRPCC). The linear post-cracking stress-crack opening correlation represents the behaviour of SFRPCC at the serviceability limit state (SLS), which is assumed to be elastoplastic in uniaxial tension and elastic in uniaxial compression. At the ultimate limit state (ULS), the compressive stress is concentrated at the upper part of the cross-section and a crack opening of 2.5 mm at the lower part is considered [54].

As shown in Fig. 10b, the post-cracking stress-crack opening relationship depends on the characteristic values of the residual flexural tensile strengths f_{R1k} and f_{R3k}, corresponding to a crack mouth opening displacement (CMOD) of 0.5 mm ($CMOD_1$) and 2.5 mm ($CMOD_3$), respectively.

Once the values of the characteristic values f_{R1k} and f_{R3k} have been calculated, the tensile stress-crack opening relationships according to the *fib* Model Code 2020 can be derived, introducing the residual flexural strengths f_{Fts} and f_{Ftu}. The first represents the residual flexural strength corresponding to the serviceability limit state (SLS), *i.e.* the post-cracking strength for serviceability crack opening of 0.5 mm, while the latter represents the residual flexural strength corresponding to the ultimate limit state (ULS), *i.e.* the post-cracking strength for ultimate crack opening of 2.5 mm. The values f_{Fts} and f_{Ftu} can be calculated as follows:

$$f_{Fts} = 0.37 \cdot f_{R1k} \quad (14)$$

$$f_{Ftu} = f_{Fts} - \frac{w_u}{CMOD_3}\left(f_{Fts} - 0.57 \cdot f_{R3k} + 0.26 \cdot f_{R1k}\right) \geq 0 \quad (15)$$

where w_u = maximum crack opening accepted in structural design. In this study, a value of w_u equal to 2.5 mm is used, thus, Eq. (15) can be rewritten as follows:

Table 10
CDP model parameters available in the literature for plain PCC and the values used for SFRPCC and SFRAASC.

Parameter	Plain PCC (from the literature)	SFRPCC and SFRAASC (this study)
σ_{b0}/σ_{c0}	1.12	1.16
K_c	$0.64 \leq K_c \leq 0.80$	0.6667
Φ	$25° \leq \Phi \leq 40°$	50°
e	0.1	0.1

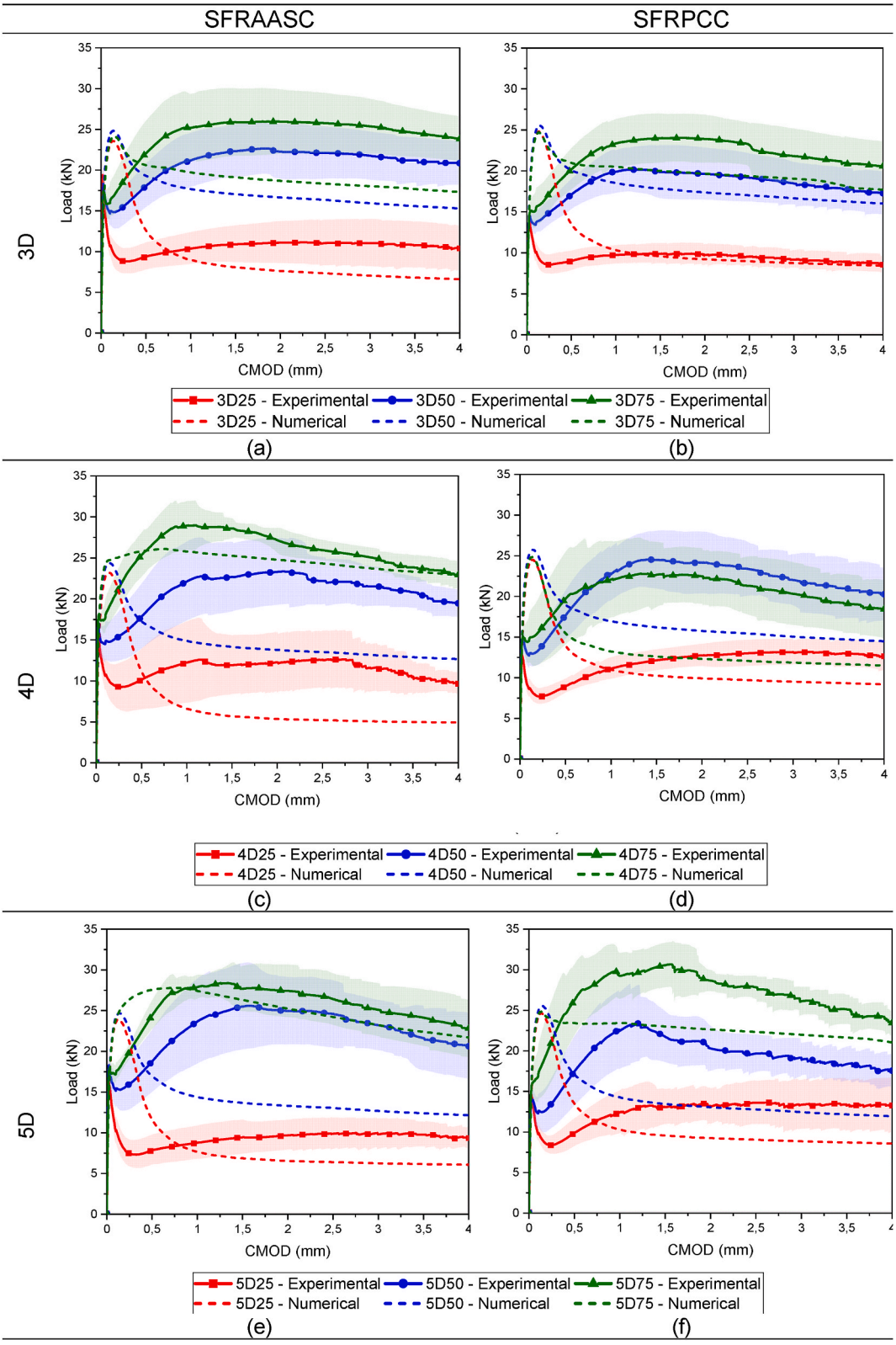

Fig. 11. Experimental and numerical Load-CMOD curve for each concrete matrix and steel fibre type.

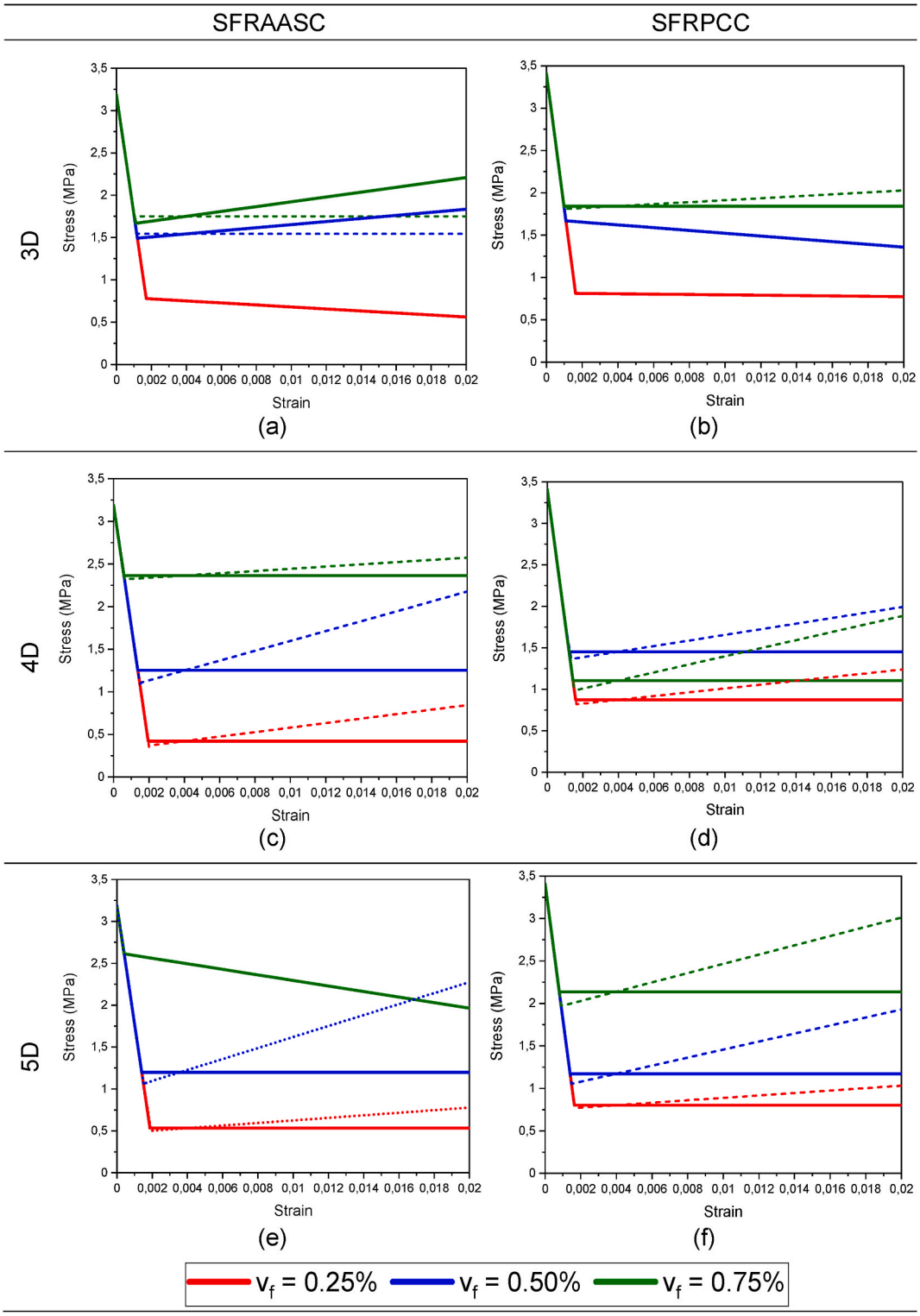

Fig. 12. Bilinear stress-strain tensile relationships for SFRAASC and SFRPCC. The dashed lines indicate the correlations obtained from the *fib* Model Code 2020 while the bold lines represent the correlations used for the numerical simulations.

$$f_{Ftu} = 0.57 \cdot f_{R3k} - 0.26 \cdot f_{R1k} \quad (16)$$

Once the values of the residual flexural strengths f_{R1} and f_{R3} and the corresponding characteristic values f_{R1k} and f_{R3k} are known, the tensile constitutive laws proposed by the *fib* Model Code 2020 can be derived for each fibre and concrete matrix type and used as input parameters for numerical simulations. From the stress-crack opening relationships, stress-strain curves can be derived according to the following equations:

$$\varepsilon_{SLS} = 0.5\ mm/l_{cs} \quad (17)$$

$$\varepsilon_{ULS} = w_u/l_{cs} \quad (18)$$

where l_{cs} is the characteristic length, which is assumed to be 125 mm in this study for each concrete matrix and fibre type.

3.4.2. Numerical simulations

The Concrete Damage Plasticity (CDP) model available in ABAQUS Software has been chosen for numerical simulations. The CDP model combines isotropic damage elasticity and isotropic compressive and tensile plasticity, allowing the prediction of the behaviour of unreinforced concrete. Although originally developed for plain cement-based concrete, several authors [55–58] applied the CDP model to fibre-reinforced concrete too, considering the composite as a homogeneous continuous material and refining the model plasticity parameters to consider the effect of fibre incorporation. These parameters, such as the ratio of the initial biaxial compressive yield stress to the initial uniaxial yield stress (σ_{b0}/σ_{c0}), the ratio of the second stress invariant on the tensile meridian to the compressive meridian at the initial yield (K_c), dilation angle (Φ) and eccentricity (e) can be obtained experimentally or they can be found in the literature for traditional cement-based concrete (PCC) with and without steel fibres [56,59–61]. The same parameters used for SFRPCC are used also for SFRAASC and they are summarised in Table 10.

Fig. 11 shows the experimental and numerical load-CMOD curves obtained for each concrete matrix and steel fibre type. For both SFRAASC and SFRPCC, the numerical model is able to capture qualitatively the post-cracking response for each fibre type and dosage. For the lowest fibre volume fraction (0.25 %), the numerical model can predict quite accurately the post-peak response of both composites. However, the peak load is overestimated, suggesting an over-prediction of the tensile strength by the constitutive model. At higher fibre volume fractions the numerical results underestimate the post-peak behaviour for both composites and all fibre types. Improving the tensile constitutive law does not necessarily lead to better numerical predictions, as demonstrated through inverse analysis in Appendix A. This suggests the inability of the CDP model to account for post-peak hardening behaviour in tension regime as shown in Fig. 11 due to theoretical limitations. As a result, the effective post-peak tensile behaviour (dashed lines in Fig. 12) has been approximated in most cases with a flatter slop as input parameter for numerical simulations. To capture the experimental post-peak hardening behaviour, discrete models explicitly accounting for fibre geometry, orientation and distribution, as the one developed by Zhang et al. [62], should be used.

4. Conclusions

This study evaluated the post-cracking flexural behaviour of steel fibre-reinforced alkali-activated slag-based concrete (SFRAASC) and same strength-grade steel fibre-reinforced cement-based concrete (SFRPCC) incorporating single (3D) and multiple (4D and 5D) hooked-end steel fibres in different volume fractions up to 0.75 %. From the experimental Load-CMOD curves, the values of the residual flexural strength f_{R1} and f_{R3} corresponding to CMOD values of 0.5 mm and 2.5 mm, respectively, have been derived. Such values have been then used to verify the applicability to SFRAASC of currently available empirical models developed for SFRPCC to predict the values of the residual strengths f_{R1} and f_{R3} by knowing the properties of the reference concrete matrix and the fibre geometry and volume fraction. Additionally, the values of f_{R1} and f_{R3} have been used to derive tensile stress-crack opening constitutive models for finite element numerical simulations. The concrete damage plasticity (CDP) model available in ABAQUS Software has been used to simulate the post-cracking behaviour of each composite. Based on the experimental and numerical investigations carried out in this study, the following conclusions can be drawn:

- The incorporation of single (3D) and multiple (4D and 5D) hooked-end steel fibres in different volume fractions has a limited effect on the flexural strength corresponding to the limit of proportionality (f_{LOP}) for both SFRAASC and SFRPCC, as it mainly depends on the mechanical behaviour of concrete matrix. However, SFRAASC mixes exhibit higher values of f_{LOP} than SFRPCC for each fibre type and volume fraction, resulting in higher resistance to flexural loading of the alkali-activated slag-based concrete matrix in comparison to a similar strength-grade cement-based concrete.
- The post-peak residual flexural strengths f_{R1} and f_{R3}, corresponding to a CMOD of 0.5 mm and 2.5 mm, respectively, increase with the increase in the fibre volume fraction for each fibre and concrete matrix type. SFRAASC mixes incorporating 3D fibres show higher values of residual flexural strengths in comparison to SFRPCC mixes incorporating the same fibre type and dosage. Although

SFRAASC and SFRPCC mixes incorporating 4D fibres in different volume fractions exhibit similar post-cracking behaviour, SFRPCC mixes incorporating 5D fibres outperform SFRAASC mixes incorporating the same fibres in the same volume fractions.

- The currently available empirical models for SFRPCC predicting the residual flexural strengths f_{R1} and f_{R3} generally overestimate the values of residual flexural strengths of SFRAASC and therefore need to be recalibrated. The empirical equations proposed by Venkateshwaran et al. [11] show the highest accuracy in predicting the residual flexural strengths of SFRAASC, thus, the equations coefficients have been recalibrated using the experimental data generated in this study and new empirical correlations have been proposed.
- The Concrete Damage Plasticity (CDP) model available in ABAQUS Software together with the *fib* Model Code 2020 qualitatively captures the behaviour of SFRAASC and SFRPCC composites incorporating single and multiple hooked-end steel fibres. However, the model proposed by the *fib* Model Code 2020 overestimate the composite peak stress. Additionally, the numerical model underestimates its post-peak behaviour, when fibre volume fractions higher than 0.25 % are used as post-cracking hardening behaviour is not accounted for in the CDP model. In summary, for higher fibre content the numerical model fails to quantitatively capture the experimental results. This is due to inherit theoretical limitation of the CDP model to account for the tensile post-cracking hardening behaviour.

This study is a first step in evaluating and understanding the post-cracking behaviour of steel fibre-reinforced alkali-activated concrete (SFRAASC) highlighting its potential as an alternative to SFRPCC for structural applications. However, further investigations are needed. Single and multiple hooked-end steel fibres should be incorporated in alkali-activated slag-based concretes of different strength grades to evaluate the effect of the concrete matrix properties on the performance of the composite. Furthermore, the fibre-matrix bond interaction should also be investigated to evaluate its effect on the flexural response of the composite. The post-cracking response of the composite, the concrete matrix properties and the fibre-matrix bond strength can then be used as input parameters for numerical simulations. Modelling each steel fibre explicitly can help to alleviate shortcomings of code-based constitutive models, as shown in this study.

CRediT authorship contribution statement

Laura Rossi: Writing – original draft, Validation, Methodology, Investigation, Formal analysis, Conceptualization. **Maria Paula Zappitelli:** Writing – original draft, Visualization, Software, Methodology, Formal analysis, Conceptualization. **Ravi A. Patel:** Writing – review & editing, Supervision, Methodology, Formal analysis, Conceptualization. **Frank Dehn:** Writing – review & editing, Supervision, Resources, Funding acquisition.

Declaration of competing interest

The authors declare that they have no known competing financial interests or personal relationships that could have appeared to influence the work reported in this paper.

Acknowledgements

This project has received funding from the European Union's Horizon 2020 research and innovation programme under grant agreement No 813596 DuRSAAM. The opinions expressed in this document reflect only the author's view and reflect in no way the European Commission's opinions. The European Commission is not responsible for any use that may be made of the information it contains.

Appendix

Numerical inverse analysis

After evaluating the applicability of the tensile constitutive model proposed by the *fib* Model Code 2020 to SFRAASC, inverse analysis was also used to derive a new tensile stress-displacement relationship as input parameter for finite element simulations to improve the accuracy of prediction. A trilinear tensile softening relationship was used for inverse analysis, as shown in Figure A.1.

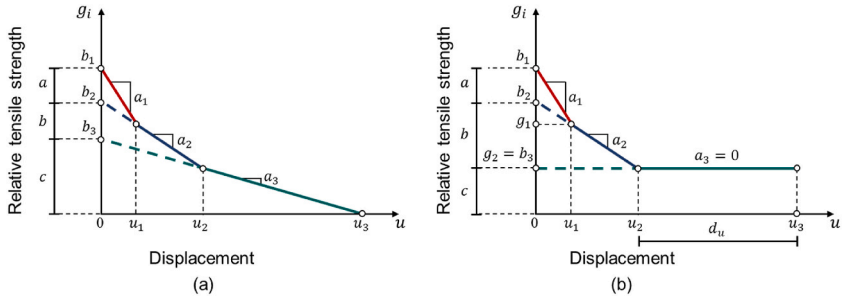

Fig. A.1. Tensile post-cracking trilinear stress-displacement curve used for (a) plain and (b) fibre-reinforced concrete, for both SFRPCC and SFRAASC.

The trilinear softening law is defined by non-dimensional parameters (g_i) obtained by normalising the tensile stress σ with the tensile strength f_t. Each segment of the trilinear curve is defined by two parameters, a_i and b_i, which represent the slope of the segment and its intercept with the y-axis, respectively.

The equations describing each segment are presented in Eq. (A.1) [43,63]:

$$g_i(u) = \frac{\sigma_i(u)}{f_t} = b_i - a_i \cdot u = \begin{cases} 1 - a_1 \cdot u, 0 \le u \le u_1 \\ b_2 - a_2 \cdot u, u_1 \le u \le u_2 \\ b_3 - a_3 \cdot u, u_2 \le u \le u_3 \end{cases} \tag{A.1}$$

The parameters to be optimized are b_i ($i = 2, 3$) and a_i ($i = 1, 2, 3$) for plain concrete. For steel fibre-reinforced concrete, the slope of the third segment is considered zero [68] and the displacement u_3 is increasing to a value d_u. To improve the definition of the bounds in the optimisation, b_i ($i = 2, 3$) parameters are not directly optimized. Instead, the parameters a, b and c (Fig. 2) are introduced. Clearly:

$$a + b + c = 1 \tag{A.2}$$

The number of optimisation parameters can be further reduced by introducing additional parameters α and β, correlating the parameters a, b and c as follows:

$$\alpha = \frac{a}{b}$$

$$\beta = \frac{b}{c} \tag{A.3}$$

Thus, replacing equation (A.2) and (A.3) in (A.1), b_i can be written depending on α and β (Eq. (A.4)):

$$b_2 = 1 - \alpha \cdot \left(\frac{1}{1 + \alpha + \beta}\right)$$

$$b_3 = 1 - (\alpha + \beta) \cdot \left(\frac{1}{1 + \alpha + \beta}\right) \tag{A.4}$$

Only the parameters α, β, a_i ($i = 1, 2, 3$) and d_u need to be optimized through inverse analysis. Global optimisation is performed using a differential evolution algorithm of the SciPy package [69]. The objective function for minimization is the difference between the load-CMOD curve obtained from numerical simulations and experiments. To have meaningful results bounds for the parameters to be optimized are given as follows:

$$a_1 \in [1, 1000],\ a_2 \in [0.1, 10],\ \alpha,\ \beta \in [0.1, 0.95],\ d_u \in [3, 5],\ \text{and}\ f_t \in [2, 4]$$

The experimental three-point bending tests performed for each concrete type (AASC and PCC) incorporating different fibre types (3D, 4D and 5D) at different volume fractions (0 %, 0.25 %, 0.50 % and 0.75 %) are modelled in ABAQUS/Explicit, considering symmetry in the middle of the notched beam. Horizontal and vertical displacements are constrained in the supports at the ends of the beam. The loading is applied as a vertical displacement along the symmetry axis of the beam. The performed analysis was quasi-static, thus, mass scaling was included to accelerate the analysis time. A quadrilateral mesh with CP4SR (four-node bilinear plane stress quadrilateral, reduced integration) elements was used. The element spacing considered was 8 mm, resulting in 662 elements.

Figure A.2 shows the output from inverse analysis and its comparison with the experimental load-CMOD curves obtained for SFRAASC and SFRPCC. The results obtained from inverse analysis are able to qualitatively capture the experimental curves for both the pre-and post-cracking phases. In terms of quantitative evaluation, the model predictions and the experimental results agree well for the reference mix and the mixes incorporating 0.25 % fibre volume fraction for both SFRAASC and SFRPCC. For higher fibre contents, significant differences exist between the numerical model and the experimental load-CMOD curves. This is mainly due to the assumption in the CDP model of a homogeneous material, *i.e.* the steel fibres and the concrete matrix are not modelled separately. Furthermore, continuum damage mechanics suffers from theoretical limitation due to the assumption of monotonically decreasing values for the post-peak tensile stress-displacement function. This is contradictory to the real behaviour of SFRAAC and SFRPCC with

higher fibre volume fractions, for which a post-cracking hardening behaviour can be observed.

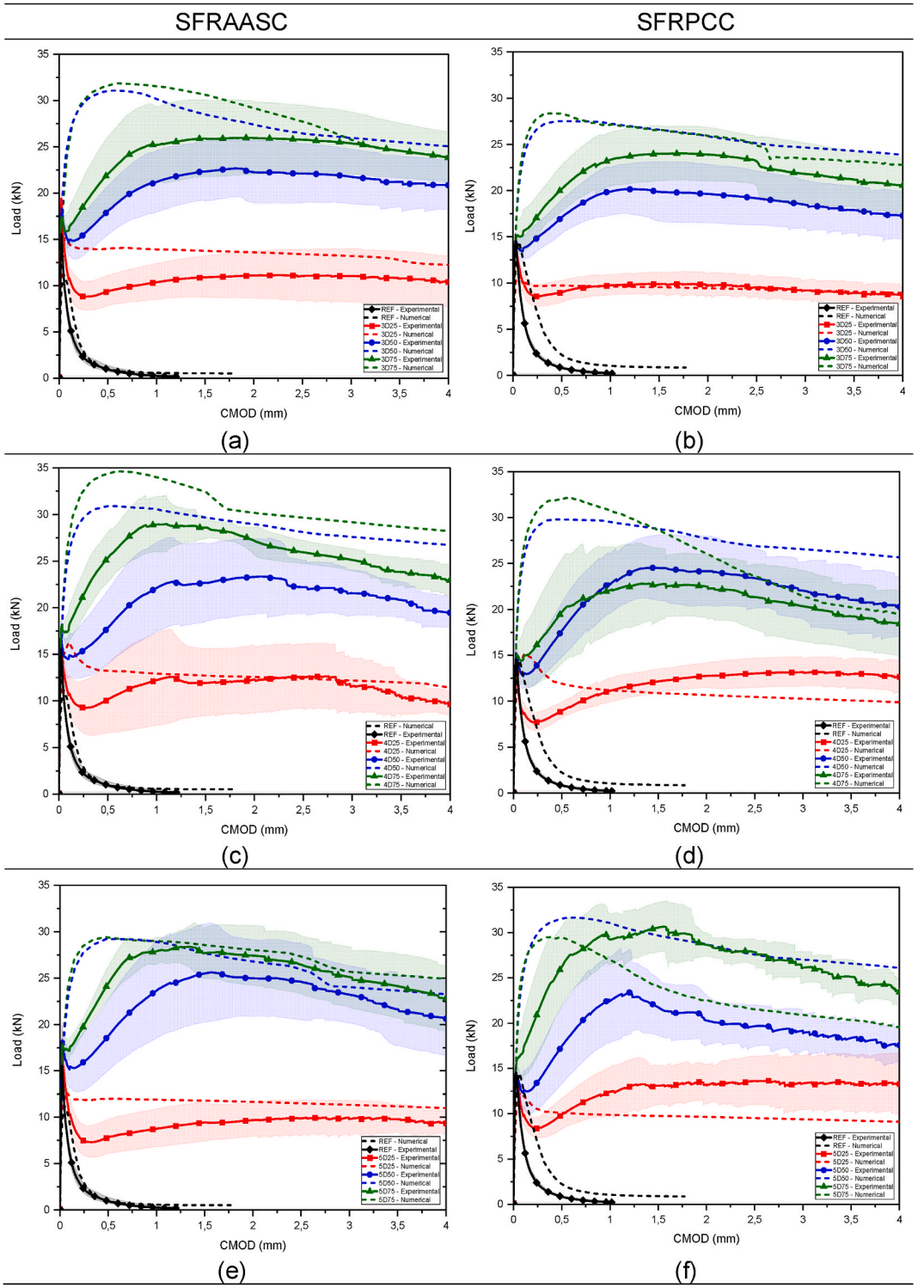

Fig. A.2. Experimental and numerical (dashed lines) load-CMOD curves for SFRAASC and SFRPCC mixes incorporating (a-b) 3D, (c-d) 4D, and (e-f) 5D steel fibres in different volume fractions.

Data availability

Data will be made available on request.

References

[1] A. Adesina, Performance of fibre reinforced alkali-activated composites – a review, Materialia 12 (Jan. 2020) 100782, https://doi.org/10.1016/j.mtla.2020.100782.

[2] G. Chen, D. Gao, H. Zhu, J. Song Yuan, X. Xiao, W. Wang, Effects of novel multiple hooked-end steel fibres on flexural tensile behaviour of notched concrete beams with various strength grades, Structures 33 (Jan. 2021) 3644–3654, https://doi.org/10.1016/j.istruc.2021.06.016.

[3] S. Guler, Z.F. Akbulut, Residual strength and toughness properties of 3D, 4D and 5D steel fiber-reinforced concrete exposed to high temperatures, Construct. Build. Mater. 327 (Jan. 2022) 126945, https://doi.org/10.1016/j.conbuildmat.2022.126945.

[4] D. joo Kim, A.E. Naaman, S. El-Tawil, Comparative flexural behavior of four fiber reinforced cementitious composites, Cem. Concr. Compos. 30 (10) (Jan. 2008) 917–928, https://doi.org/10.1016/j.cemconcomp.2008.08.002.

[5] B. Li, L. Xu, Y. Shi, Y. Chi, Q. Liu, C. Li, Effects of fiber type, volume fraction and aspect ratio on the flexural and acoustic emission behaviors of steel fiber reinforced concrete, Construct. Build. Mater. 181 (Jan. 2018) 474–486, https://doi.org/10.1016/j.conbuildmat.2018.06.065.

[6] A. Enfedaque, M.G. Alberti, J.C. Gálvez, P. Cabanas, Numerical simulation of the fracture behavior of high-performance fiber-reinforced concrete by using a cohesive crack-based inverse analysis, Mater. Basel Switz. 15 (1) (Jan. 2021), https://doi.org/10.3390/ma15010071.

[7] S. Abdallah, M. Fan, X. Zhou, Pull-out behaviour of hooked end steel fibres embedded in ultra-high performance mortar with various W/B ratios, Int. J. Concr. Struct. Mater. 11 (2) (Jan. 2017) 301–313, https://doi.org/10.1007/s40069-017-0193-8.

[8] F.U.A. Shaikh, Y. Shafaei, P.K. Sarker, Effect of nano and micro-silica on bond behaviour of steel and polypropylene fibres in high volume fly ash mortar, Construct. Build. Mater. 115 (Jan. 2016) 690–698, https://doi.org/10.1016/j.conbuildmat.2016.04.090.

[9] S. Abdallah, M. Fan, X. Zhou, S. Le Geyt, Anchorage effects of various steel fibre architectures for concrete reinforcement, Int. J. Concr. Struct. Mater. 10 (3) (Jan. 2016) 325–335, https://doi.org/10.1007/s40069-016-0148-5.

[10] G. Tiberti, F. Germano, A. Mudadu, G.A. Plizzari, An overview of the flexural post-cracking behavior of steel fiber reinforced concrete, Struct. Concr. 19 (3) (Jan. 2018) 695–718, https://doi.org/10.1002/suco.201700068.

[11] A. Venkateshwaran, K.H. Tan, Y. Li, Residual flexural strengths of steel fiber reinforced concrete with multiple hooked-end fibers, Struct. Concr. 19 (2) (Jan. 2018) 352–365, https://doi.org/10.1002/suco.201700030.

[12] M. Amran, et al., Fiber-reinforced alkali-activated concrete: a review, J. Build. Eng. 45 (Jan. 2022) 103638, https://doi.org/10.1016/j.jobe.2021.103638.

[13] Y. Ding, J.-G. Dai, C.-J. Shi, Fracture properties of alkali-activated slag and ordinary Portland cement concrete and mortar, Construct. Build. Mater. 165 (Jan. 2018) 310–320, https://doi.org/10.1016/j.conbuildmat.2017.12.202.

[14] Y. Du, J. Wang, C. Shi, H.-J. Hwang, N. Li, Flexural behavior of alkali-activated slag-based concrete beams, Eng. Struct. 229 (Jan. 2021) 111644, https://doi.org/10.1016/j.engstruct.2020.111644.

[15] H.-J. Lim, C.-G. Cho, J.-Y. You, J.-J. Jeong, Mechanical properties of alkali-activated slag fiber composites varying with fiber volume fractions, Mater. Basel Switz 15 (18) (Jan. 2022), https://doi.org/10.3390/ma15186444.

[16] Ü. Yurt, An experimental study on fracture energy of alkali activated slag composites incorporated different fibers, J. Build. Eng. 32 (Jan. 2020) 101519, https://doi.org/10.1016/j.jobe.2020.101519.

[17] S. Bernal, R. Mejía de Gutiérrez, E. Rodríguez, S. Delvasto, F. Puertas, Mechanical behaviour of steel fibre-reinforced alkali activated slag concrete, Mater. Constr. 59 (293) (Jan. 2009) 53–62, https://doi.org/10.3989/mc.2009.41807.

[18] N. Ranjbar, M. Zhang, Fiber-reinforced geopolymer composites: a review, Cem. Concr. Compos. 107 (Jan. 2020) 103498, https://doi.org/10.1016/j.cemconcomp.2019.103498.

[19] H. El-Hassan, S. Elkholy, Enhancing the performance of Alkali-Activated Slag-Fly ash blended concrete through hybrid steel fiber reinforcement, Construct. Build. Mater. 311 (Jan. 2021) 125313, https://doi.org/10.1016/j.conbuildmat.2021.125313.

[20] A. Adesina, S. Das, Drying shrinkage and permeability properties of fibre reinforced alkali-activated composites, Construct. Build. Mater. 251 (Jan. 2020) 119076, https://doi.org/10.1016/j.conbuildmat.2020.119076.

[21] M.H. Al-Majidi, A. Lampropoulos, A.B. Cundy, Steel fibre reinforced geopolymer concrete (SFRGC) with improved microstructure and enhanced fibre-matrix interfacial properties, Construct. Build. Mater. 139 (Jan. 2017) 286–307, https://doi.org/10.1016/j.conbuildmat.2017.02.045.

[22] N.P. Asrani, et al., A feasibility of enhancing the impact resistance of hybrid fibrous geopolymer composites: experiments and modelling, Construct. Build. Mater. 203 (Jan. 2019) 56–68, https://doi.org/10.1016/j.conbuildmat.2019.01.072.

[23] S. Aydın, B. Baradan, The effect of fiber properties on high performance alkali-activated slag/silica fume mortars, Compos. Part B Eng. 45 (1) (Jan. 2013) 63–69, https://doi.org/10.1016/j.compositesb.2012.09.080.

[24] K. Behfarnia, M. Rostami, Mechanical properties and durability of fiber reinforced alkali activated slag concrete, J. Mater. Civ. Eng. 29 (12) (Jan. 2017) 04017231, https://doi.org/10.1061/(ASCE)MT.1943-5533.0002073.

[25] S. Bernal, R. Gutierrez, S. Delvasto, E. Rodriguez, Performance of an alkali-activated slag concrete reinforced with steel fibers, Construct. Build. Mater. 24 (2) (Jan. 2010) 208–214, https://doi.org/10.1016/j.conbuildmat.2007.10.027.

[26] J.-I. Choi, B.Y. Lee, R. Ranade, V.C. Li, Y. Lee, Ultra-high-ductile behavior of a polyethylene fiber-reinforced alkali-activated slag-based composite, Cem. Concr. Compos. 70 (Jan. 2016) 153–158, https://doi.org/10.1016/j.cemconcomp.2016.04.002.

[27] S.-J. Choi, J.-I. Choi, J.-K. Song, B.Y. Lee, Rheological and mechanical properties of fiber-reinforced alkali-activated composite, Construct. Build. Mater. 96 (Jan. 2015) 112–118, https://doi.org/10.1016/j.conbuildmat.2015.07.182.

[28] H. El-Hassan, S. Elkholy, Performance evaluation and microstructure characterization of steel fiber–reinforced alkali-activated slag concrete incorporating fly ash, J. Mater. Civ. Eng. 31 (10) (Jan. 2019), https://doi.org/10.1061/(ASCE)MT.1943-5533.0002872, 04019223 vols.

[29] K.Z. Farhan, M.A.M. Johari, R. Demirboğa, Impact of fiber reinforcements on properties of geopolymer composites: a review, J. Build. Eng. 44 (Jan. 2021) 102628, https://doi.org/10.1016/j.jobe.2021.102628.

[30] N.A. Farhan, M.N. Sheikh, M.N.S. Hadi, Engineering properties of ambient cured alkali-activated fly ash–slag concrete reinforced with different types of steel fiber, J. Mater. Civ. Eng. 30 (7) (Jan. 2018), https://doi.org/10.1061/(ASCE)MT.1943-5533.0002333, 04018142 vols.

[31] N. Ganesan, R. Abraham, S. Deepa Raj, Durability characteristics of steel fibre reinforced geopolymer concrete, Construct. Build. Mater. 93 (Jan. 2015) 471–476, https://doi.org/10.1016/j.conbuildmat.2015.06.014.

[32] X. Guo, X. Pan, Mechanical properties and mechanisms of fiber reinforced fly ash–steel slag based geopolymer mortar, Construct. Build. Mater. 179 (Jan. 2018) 633–641, https://doi.org/10.1016/j.conbuildmat.2018.05.198.

[33] N. Hammad, A. El-Nemr, H. El-Deen Hasan, The performance of fiber GGBS based alkali-activated concrete, J. Build. Eng. 42 (Jan. 2021) 102464, https://doi.org/10.1016/j.jobe.2021.102464.

[34] A. Koenig, et al., Flexural behaviour of steel and macro-PP fibre reinforced concretes based on alkali-activated binders, Construct. Build. Mater. 211 (Jan. 2019) 583–593, https://doi.org/10.1016/j.conbuildmat.2019.03.227.

[35] C.K. Lau, T.N.S. Htut, J.J. Melling, A. Chegenizadeh, T.S. Ng, Torsional behaviour of steel fibre reinforced alkali activated concrete, Mater. Basel Switz. 13 (15) (Jan. 2020), https://doi.org/10.3390/ma13153423.

[36] Q. Meng, et al., Steel fibre reinforced alkali-activated geopolymer concrete slabs subjected to natural gas explosion in buried utility tunnel, Construct. Build. Mater. 246 (Jan. 2020) 118447, https://doi.org/10.1016/j.conbuildmat.2020.118447.

[37] B. Nematollahi, J. Sanjayan, F.U.A. Shaikh, Matrix design of strain hardening fiber reinforced engineered geopolymer composite, Compos. Part B Eng. 89 (Jan. 2016) 253–265, https://doi.org/10.1016/j.compositesb.2015.11.039.
[38] B. Nematollahi, J. Sanjayan, F.U.A. Shaikh, Comparative deflection hardening behavior of short fiber reinforced geopolymer composites, Construct. Build. Mater. 70 (Jan. 2014) 54–64, https://doi.org/10.1016/j.conbuildmat.2014.07.085.
[39] F.U.A. Shaikh, Review of mechanical properties of short fibre reinforced geopolymer composites, Construct. Build. Mater. 43 (Jan. 2013) 37–49, https://doi.org/10.1016/j.conbuildmat.2013.01.026.
[40] K. Zada Farhan, M. Azmi Megat Johari, R. Demirboğa, Evaluation of properties of steel fiber reinforced GGBFS-based geopolymer composites in aggressive environments, Construct. Build. Mater. 345 (Jan. 2022) 128339, https://doi.org/10.1016/j.conbuildmat.2022.128339.
[41] X. Zhou, Y. Zeng, P. Chen, Z. Jiao, W. Zheng, Mechanical properties of basalt and polypropylene fibre-reinforced alkali-activated slag concrete, Construct. Build. Mater. 269 (Jan. 2021) 121284, https://doi.org/10.1016/j.conbuildmat.2020.121284.
[42] F.U.A. Shaikh, Pullout behavior of hook end steel fibers in geopolymers, J. Mater. Civ. Eng. 31 (6) (Jan. 2019) 04019068, https://doi.org/10.1061/(ASCE)MT.1943-5533.0002722.
[43] D. Gao, C. Ding, Y. Pang, G. Chen, An inverse analysis method for multi-linear tensile stress-crack opening relationship of 3D/4D/5D steel fiber reinforced concrete, Construct. Build. Mater. 309 (Jan. 2021) 125074, https://doi.org/10.1016/j.conbuildmat.2021.125074.
[44] O. Sucharda, M. Pajak, T. Ponikiewski, P. Konecny, Identification of mechanical and fracture properties of self-compacting concrete beams with different types of steel fibres using inverse analysis, Construct. Build. Mater. 138 (Jan. 2017) 263–275, https://doi.org/10.1016/j.conbuildmat.2017.01.077.
[45] S.J. Stephen, B. Raphael, R. Gettu, S. Jose, Determination of the tensile constitutive relations of fiber reinforced concrete using inverse analysis, Construct. Build. Mater. 195 (Jan. 2019) 405–414, https://doi.org/10.1016/j.conbuildmat.2018.11.014.
[46] L.M.P. Matos, J.A.O. Barros, A. Ventura-Gouveia, R.A.B. Calçada, A new inverse analysis approach for predicting the fracture mode I parameters of fibre reinforced concrete, Eng. Fract. Mech. 246 (Jan. 2021) 107613, https://doi.org/10.1016/j.engfracmech.2021.107613.
[47] fib Model Code for Concrete Structures (2020), Version 1. Lausanne: International Federation of Structural Concrete, 2023.
[48] L. Rossi, R.A. Patel, F. Dehn, Compressive behaviour of alkali-activated slag-based concrete and Portland cement concrete incorporating novel multiple hooked-end steel fibres, Mater. Struct. 56 (5) (Jan. 2023), https://doi.org/10.1617/s11527-023-02180-2.
[49] L. Rossi, et al., Future perspectives for alkali-activated materials: from existing standards to structural applications, RILEM Tech. Lett. 7 (Jan. 2022) 159–177, https://doi.org/10.21809/rilemtechlett.2022.160.
[50] S.-J. Lee, D.-Y. Yoo, D.-Y. Moon, Effects of hooked-end steel fiber geometry and volume fraction on the flexural behavior of concrete pedestrian decks, Appl. Sci. 9 (6) (Jan. 2019) 1241, https://doi.org/10.3390/app9061241.
[51] E. Faccin, L. Facconi, F. Minelli, G. Plizzari, Predicting the residual flexural strength of concrete reinforced with hooked-end steel fibers: new empirical equations, in: P. Serna, A. Llano-Torre, J.R. Martí-Vargas, J. Navarro-Gregori (Eds.), Fibre Reinforced Concrete: Improvements and Innovations II, vol. 36, Springer International Publishing, Cham, 2022, pp. 456–468, https://doi.org/10.1007/978-3-030-83719-8_40, in RILEM Bookseries, vol. 36.
[52] B.N. Moraes Neto, J.A.O. Barros, G.S.S.A. Melo, Model to simulate the contribution of fiber reinforcement for the punching resistance of RC slabs, J. Mater. Civ. Eng. 26 (7) (Jul. 2014) 04014020, https://doi.org/10.1061/(ASCE)MT.1943-5533.0000913.
[53] V. Oettel, M. Schulz, M. Haist, Empirical approach for the residual flexural tensile strength of steel fiber-reinforced concrete based on notched three-point bending tests, Struct. Concr. 23 (2) (Apr. 2022) 993–1004, https://doi.org/10.1002/suco.202100565.
[54] M. Di Prisco, M. Colombo, D. Dozio, Fibre-reinforced concrete in fib Model Code 2010: principles, models and test validation, Struct. Concr. 14 (4) (Dec. 2013) 342–361, https://doi.org/10.1002/suco.201300021.
[55] N. Belyakov, O. Smirnova, A. Alekseev, H. Tan, Numerical simulation of the mechanical behavior of fiber-reinforced cement composites subjected dynamic loading, Appl. Sci. 11 (3) (Jan. 2021) 1112, https://doi.org/10.3390/app11031112.
[56] Y. Chi, M. Yu, Le Huang, L. Xu, Finite element modeling of steel-polypropylene hybrid fiber reinforced concrete using modified concrete damaged plasticity, Eng. Struct. 148 (Jan. 2017) 23–35, https://doi.org/10.1016/j.engstruct.2017.06.039.
[57] H. Othman, H. Marzouk, Applicability of damage plasticity constitutive model for ultra-high performance fibre-reinforced concrete under impact loads, Int. J. Impact Eng. 114 (Jan. 2018) 20–31, https://doi.org/10.1016/j.ijimpeng.2017.12.013.
[58] T. Tysmans, M. Wozniak, O. Remy, J. Vantomme, Finite element modelling of the biaxial behaviour of high-performance fibre-reinforced cement composites (HPFRCC) using Concrete Damaged Plasticity, Finite Elem. Anal. Des. 100 (Jan. 2015) 47–53, https://doi.org/10.1016/j.finel.2015.02.004.
[59] T. Jankowiak, T. Łodygowski, Identification of parameters of concrete damage plasticity constitutive model, Found. Civ. Environ. Eng. 6 (Jan. 2005) 53–69.
[60] J. Lee, G.L. Fenves, Plastic-damage model for cyclic loading of concrete structures, J. Eng. Mech. 124 (8) (Jan. 1998) 892–900, https://doi.org/10.1061/(ASCE)0733-9399(1998)124:8(892).
[61] J. Lubliner, J. Oliver, S. Oller, E. Oñate, A plastic-damage model for concrete, Int. J. Solid Struct. 25 (3) (Jan. 1989) 299–326, https://doi.org/10.1016/0020-7683(89)90050-4.
[62] H. Zhang, Y.J. Huang, Z.J. Yang, S.L. Xu, X.W. Chen, A discrete-continuum coupled finite element modelling approach for fibre reinforced concrete, Cement Concr. Res. 106 (Apr. 2018) 130–143, https://doi.org/10.1016/j.cemconres.2018.01.010.
[63] J.F. Olesen, Fictitious crack propagation in fiber-reinforced concrete beams, J. Eng. Mech. 127 (3) (Jan. 2001) 272–280, https://doi.org/10.1061/(ASCE)0733-9399(2001)127:3(272).